

Classical and Quantum Simulation of Electron Transfer Through a Polypeptide

Lowell W. Ungar,[†] Marshall D. Newton,^{*,‡} and Gregory A. Voth^{*,†}

Department of Chemistry and Henry Eyring Center for Theoretical Chemistry, University of Utah, Salt Lake City, Utah, and Chemistry Department, Brookhaven National Laboratory, Upton, New York

Received: March 26, 1999; In Final Form: June 8, 1999

Quantum rate theory, molecular dynamics simulations, and semiempirical electronic structure calculations are used to fully investigate electron transfer mediated by a solvated polypeptide for the first time. Using a stationary-phase approximation, the nonadiabatic electron-transfer rate constant is calculated from the nuclear free energies and the electronic coupling between the initial and final states. The former are obtained from quantum path integral and classical molecular dynamics simulations; the latter are calculated using semiempirical electronic structure calculations and the generalized Mulliken–Hush method. Importantly, no parameters are fit to kinetic data. The simulated system consists of a solvated four-proline polypeptide with a tris(bipyridine)ruthenium donor group and an oxypentamminecobalt acceptor group. From the simulation data entropy and energy contributions to the free energies are distinguished. Quantum suppression of the barrier, including important solvent contributions, is demonstrated. Although free energy profiles along the reaction coordinate are nearly parabolic, pronounced departures from harmonic behavior are found for the separate energy and entropy functions. Harmonic models of the system are compared to simulation results in order to quantify anharmonic effects. Electronic structure calculations show that electronic coupling elements vary considerably with system conformation, even when the effective donor–acceptor separation remains roughly constant. The calculations indicate that electron transfer in a significant range of conformations linking the polypeptide to the acceptor may contribute to the overall rate constant. After correction for limitations of the solvent model, the simulations and calculations agree well with the experimental activation energy and Arrhenius prefactor.

I. Introduction

Activated electron transfer between widely separated local donor and acceptor sites is a process of major importance in many areas of chemistry, physics, and biology.¹ In biology, long-range electron transfer (over tens of Ångströms) plays a key role in energy transport, most notably in photosynthesis and respiration. The electron transfer can be considered a transition between electronic states, the rate of which is determined both by the coupling between the electronic states and by the nuclear fluctuations necessary to bring the states into resonance so that energy is conserved during the transfer. Although the electron motion is effectively instantaneous on the time scale of nuclear motions, the rate of activated electron transfer is usually slow on that time scale. Rate constants can vary over many orders of magnitude as a result of the roughly exponential dependence of the nuclear population density on the system potential energy and of the electronic-state overlap on the donor–acceptor separation. Reliable simulation of the nuclear fluctuations and free energies and calculation of the electronic states and couplings, both necessary to understand the electron-transfer kinetics, pose a major challenge to theoretical and computational chemistry.

Early theoretical work on electron-transfer rates showed that, in classical systems with free energy curves that are parabolic functions of an electron-transfer reaction coordinate, rates have a simple exponential dependence on the activation free energy (the reaction barrier), which in turn depends on the reaction

and reorganization free energies.^{1,2} The electron-transfer coordinate is a collective nuclear coordinate describing the nuclear motions that accompany the electron transfer, generally taken to be the vertical potential energy difference between the initial and final electronic states. If the potential energy surfaces for the initial and final electronic states are known, then molecular dynamics simulations with biased potentials (umbrella sampling³) can be used to calculate the necessary free energies. If the electronic coupling between initial and final states is small (nonadiabatic limit), it appears explicitly in the rate constant prefactor. Although the coupling often is treated as an adjustable parameter, which may be allowed to vary exponentially with the donor–acceptor separation, but which otherwise does not vary with nuclear coordinates (the Condon approximation⁴), it is highly desirable to calculate the coupling directly, preferably over a broad range of coordinates.

In quantum systems the effective reaction barrier may be lowered by nuclear tunneling. Early theories obtained analytical expressions for the quantum effects using a displaced harmonic model.⁵ In the nonadiabatic limit one can use the stationary phase approximation to derive a quantum rate expression for arbitrary potential surfaces, analogous to the familiar Marcus classical picture.^{6–8} An equivalent expression was also obtained from a more general unstable-mode picture of electron transfer.⁹ The necessary free energy differences and derivatives can be calculated using path integral molecular dynamics methods, which yield quantum equilibrium properties from a classical molecular dynamics simulation. A similar approach has been used to calculate the activation free energy for aqueous electron exchange (electron transfer between sites identical except for

[†] University of Utah.

[‡] Brookhaven National Laboratory.

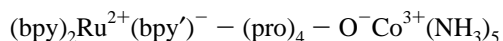
the oxidation state): $\text{Fe}^{2+/3+}$,¹⁰ $\text{Co}(\text{NH}_3)_6^{2+/3+}$,¹¹ and cytochrome *c*.¹² A complete kinetic model, however, requires evaluation of the electronic coupling (e.g., see ref 13).

In this paper we calculate both the free energy and the electronic coupling quantities for electron transfer in a model (synthetic) biological system. The free energies are found using both classical and path integral molecular dynamics simulations. Semiempirical electronic structure calculations are used with the generalized Mulliken–Hush method¹⁴ to obtain the electronic coupling elements. The only input parameters are thus from the molecular mechanics potential energy surfaces, which are fit to independent (nonkinetic) experimental data.

Using this approach we examine several factors that can affect the electron-transfer rate. Nuclear tunneling effects are isolated by calculating free energies for both quantum and classical systems. Entropic and energetic effects are distinguished by calculating energy differences as well as free energy differences. Harmonic models are compared to the simulated anharmonic system. Solute and solvent contributions to the reaction coordinate are distinguished. The Condon approximation, which is common-place in electron-transfer theories, is directly tested by semiempirical calculations with different nuclear configurations.

We also compare our results in this paper with experimental results. A detailed understanding of entropic effects is crucial in interpreting the prefactor and exponent obtained from conventional Arrhenius analysis of temperature-dependent rate constants. As the entropic contribution to the activation free energy has no exponential temperature dependence, it must be included in the Arrhenius prefactor. In the limit of nonadiabatic kinetics pertinent to the present study of long-range electron transfer, an independent estimate of the activation entropy is necessary to infer the electronic coupling from the overall prefactor (e.g., see refs 15 and 16) or the activation free energy from the exponent. Among the contributions to the activation entropy, we investigate in particular the temperature dependence of the solvent reorganization free energy, an effect which has recently received considerable attention in the literature.^{17–19}

The overall computational methodology outlined above and in the next section is tested by application to a solvated polypeptide-based system that has been used as a model in experimental investigations of electron-transfer rates.²⁰ The system consists of a polyproline peptide linking transition-metal-based electron donor (D) and acceptor (A) groups, with the entire DSA complex (the reactive “system”) immersed in aqueous solution. Specifically, the donor, spacer (peptide), and acceptor, shown in Figure 1, are as follows:



where in the donor $\text{bpy} \equiv 2,2'$ -bipyridine and $\text{bpy}' \equiv 4'$ -methyl-2,2'-bipyridyl is linked to the spacer by a carbonyl group at the C₄ position; the spacer is a polyproline chain whose first member (the N-terminus) is connected to the bpy' carbonyl by an amide linkage, and whose fourth member (the C-terminus) is terminated by a carboxylate moiety bonded (at one oxygen) to the $-\text{Co}^{3+}(\text{NH}_3)_5$ acceptor moiety. This system has been chosen for study because it is a representative member of a homologous series of systems for which experimental rates as a function of temperature have been studied by electron pulse radiolysis.^{20,21} An apparent difference between the length dependence for 1–3 prolines and for 4–6 prolines was attributed to the formation of a rigid helix with four or more prolines. It has, however, been suggested for a similar system that electron transfer would

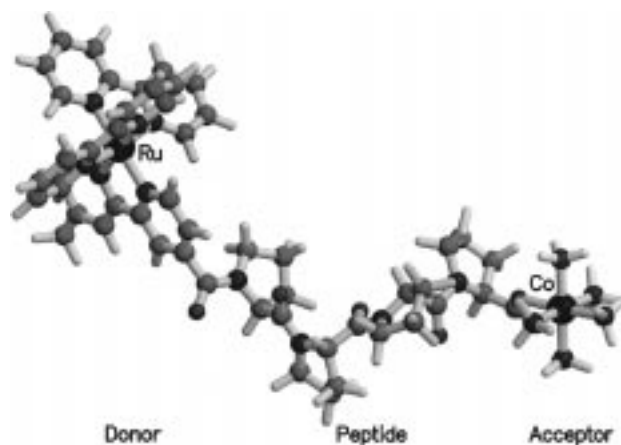


Figure 1. Diagram of the electron-transfer system studied. The peptide contains four proline amino acids, the donor is a $\text{Ru}(\text{bpy})_3$ derivative, and the acceptor is $-\text{OCo}(\text{NH}_3)_5$. In the simulations, the system is immersed in water. Image created using Molscript¹ and Raster3D.²

be faster through solvent molecules with kinked conformations of the peptide in which the donor and acceptor are much closer.²²

Electron transfer in this system should also be affected by nuclear tunneling in part because there is a large displacement of the $\text{Co}-\text{N}$ bond length upon reduction of the acceptor, causing a barrier that can be tunneled through.^{23–26} The ammonia molecules in the $\text{Co}^{2+/3+}$ coordination shell are the counterpart of the tightly bound first-shell water molecules in the aqueous $\text{Fe}^{2+/3+}$ system.^{10,27} Although the tunneling would be most pronounced if the high-spin (quartet) ground state Co^{2+} complex were formed, it is still significant for reduction yielding the low-spin (doublet) excited state.²³ In the present study we model the low-spin reaction pathway since, as inferred for related processes¹⁵ involving the reduction of Co^{3+} , the rate constant for this pathway is favored relative to the high-spin alternative because of both the activation energy and the prefactor. In the activation energy, the gain in exothermicity (-13 kcal/mol)^{28,29} would be more than offset by the expected increase in inner-sphere reorganization free energy at the Co site (a value of ~ 35 kcal/mol is expected for the high-spin case,^{1,23,24} roughly double the value for the low-spin process;^{23,25,30} as noted below, the present simulations yield a value of 16 kcal/mol for the low-spin process in the isolated DSA system). Spin-orbit coupling would be required for the high-spin pathway, which couples a doublet initial state with a quartet final state. The requirement of spin-orbit mixing is expected to lead to an attenuation factor of $\sim 10^{-3}$ in the high-spin prefactor, using a model of the type reported in ref 23.

The next section will briefly describe the necessary electron-transfer rate theory, molecular dynamics methods, and semiempirical electronic structure methods, and section III details the potential energy surfaces. Section IV presents and discusses results from the simulation and from displaced harmonic models. The calculated coupling elements for various conformations are presented in section V. In section VI the calculated results are corrected for known errors in the simulation models and compared with available estimates of kinetic parameters from experiment. Section VII concludes with mechanistic implications of the results.

II. Methods

A. Golden Rule Rate Constant. In biological and other systems with widely separated donor and acceptor sites the

electron transfer is in the nonadiabatic limit. As the coupling between the initial and final electronic diabatic states is weak, it can be treated as a small perturbation, and the electron transfer can be considered as the transition between the charge-localized (diabatic) electronic states. In the diabatic representation the Hamiltonian can be written

$$H = |i\rangle H_i \langle i| + |f\rangle H_f \langle f| + V_{if}(\mathbf{r})(|i\rangle \langle f| + |f\rangle \langle i|) \quad (1)$$

where H_i and H_f are the nuclear Hamiltonians in the electronic states i and f before and after electron transfer, respectively, and V_{if} is the weak electronic coupling, considered for the moment to be a function of the nuclear coordinates \mathbf{r} . Assuming the system starts at thermal nuclear equilibrium in the initial electronic state, the rate of electron transfer is the time derivative of the population of the final state and is assumed to plateau at long times. First-order time-dependent perturbation theory in the coupling (the golden rule) yields^{6,7}

$$k \equiv \left. \frac{dP_f(t)}{dt} \right|_{t \rightarrow \infty} = \frac{1}{\hbar^2} \int_{-\infty}^{\infty} dt \langle \exp(iH_i t/\hbar) V_{if} \exp(-iH_f t/\hbar) V_{if} \rangle_i \quad (2)$$

where P_f is the population in the final electronic state, and $\langle \cdots \rangle_i$ denotes an equilibrium average in the initial electronic state. Unfortunately, exact calculation of the integrand requires quantum real-time dynamics, which is unfeasible for large anharmonic systems.

For a classical system with free energy curves that are parabolic functions of the electron-transfer coordinate, and with electronic coupling that does not depend on the nuclear coordinates (Condon approximation⁴), this expression reduces to the standard Marcus expression for the nonadiabatic electron-transfer rate constant¹

$$k_{cl} = V_{if}^2 \frac{1}{\hbar} \sqrt{\frac{\pi\beta}{\lambda}} \exp(-\beta\Delta F^\ddagger) \quad (3)$$

where $\beta = 1/k_B T$, λ is the reorganization free energy (a measure of the coordinate displacements between the minima of the two potential energy surfaces), and ΔF^\ddagger is the activation free energy (the effective barrier to reaction). Under these ‘‘Marcus’’ conditions¹

$$\Delta F^\ddagger = \frac{(\Delta F^\circ + \lambda)^2}{4\lambda} \quad (4)$$

where ΔF° is the reaction free energy (the negative of the driving force of the reaction). The assumption of parabolic free energy curves is valid for multidimensional harmonic systems in which the potential energy surfaces are displaced but have no frequency changes or Duschinsky rotation.

An analogous expression for a quantum, anharmonic system can be derived using the stationary phase (steepest descent or saddle point) approximation. The integration in eq 2 is deformed from the real axis into the complex plane (there are no poles of the integrand to interfere) in a path chosen to cross the imaginary-time axis where the integrand is at a minimum. This point is the stationary phase point and can be considered the transition state. As the integrand at the stationary phase point is at a maximum along the integration path, its logarithm is expanded quadratically and the Gaussian integral is done analytically. In the Condon approximation the result takes the form^{8,9} (see Appendix B for more general expressions)

$$k_{sp} = V_{if}^2 \frac{1}{\hbar} \sqrt{\frac{\pi\beta}{-d^2 F/d\tau^2|_{\tau_{ts}/2}}} \exp[-\beta(F(\tau_{ts}) - F(0))] \quad (5)$$

where

$$\exp[-\beta F(\tau)] = Z(\tau) = \text{Tr}[\exp(-H_f \beta(1 - \tau)) \exp(-H_i \beta \tau)] \quad (6)$$

$$\left. \frac{dF(\tau)}{d\tau} \right|_{\tau_{ts}} = \langle \Delta V \rangle_{\tau_{ts}} = 0 \quad (7)$$

$$\frac{d^2 F(\tau)}{d\tau^2} = -\beta[\langle \Delta V(\tau) \Delta V(0) \rangle_\tau - \langle \Delta V \rangle_\tau^2] \quad (8)$$

Here, $\Delta V = H_f - H_i$ is the potential difference between the two electronic states, and

$$\langle X(\tau) Y(0) \rangle_\tau = \frac{1}{Z(\tau)} \text{Tr}[e^{-H_f \beta(1-\tau)} X e^{-H_i \beta \tau} Y] \quad (9)$$

The rate constant is defined in terms of a hybrid partition function, $Z(\tau)$, which for $\tau = 0$ is the partition function of the initial state, and for $\tau = 1$ is the partition function of the final state. The transition state is at the value of $\tau = \tau_{ts}$ for which the average of the difference potential is equal to zero, i.e., around the curve crossing. In the normal Marcus regime ($-\Delta F^\circ < \lambda$), $0 < \tau_{ts} < 1$, while in the Marcus inverted region ($-\Delta F^\circ > \lambda$), hence the curve crossing is *not* between the minima of the two free energy wells), $\tau_{ts} < 0$ if $\Delta F^\circ < 0$. The transition state is a maximum on the integration path but is not necessarily the only maximum. Thus, the stationary phase expression should be considered an ansatz rather than a rigorously justified approximation.

The parallel between eq 5 and the widely used Marcus equation should be clear: the activation free energy $\Delta F^\ddagger = F(\tau_{ts}) - F(0)$, and the reorganization free energy λ is replaced by the curvature of the free energy, $-d^2 F/d\tau^2|_{\tau_{ts}/2}$. The free energies are defined in terms of unconstrained hybrid partition functions rather than the more typical potentials of mean force (PMFs) constrained along the reaction coordinate (usually taken as ΔV), but either definition is equally valid. For a classical system with parabolic PMF curves, both definitions of the activation and reaction free energies are equivalent, and the free energy curvature is equal to the reorganization free energy. The unconstrained and the constrained free energies will be shown below in Figure 2 and Figure 3 respectively. The effective barrier to reaction is directly revealed as the maximum in the unconstrained free energy curve ($F(\tau)$). In the PMF curves ($F(x)$) the barrier is determined by the curve crossing.

As the free energy differences and derivatives in eqs 5–8 are imaginary-time quantities, taking $t = -i\hbar\beta\tau$ to be the time, they can be obtained from path integral molecular dynamics (or Monte Carlo) simulations.³¹ In path integral molecular dynamics the density operator, $\exp(-\beta H)$, is divided into P small pieces, $\exp(-\beta H/P)$, by repeated expansion in the nuclear coordinates (sometimes called ‘‘beads’’). The small operator pieces can be Trotter factorized, and the sum of the exponents forms a potential function of all the beads. Its properties can be obtained using classical molecular dynamics. With the hybrid density operator of eq 6, beads from 0 to τ move on the final-state potential and beads from τ to 1 move on the initial-state potential (except the beads nearest 0 and nearest τ which move on a linear combination of the two potentials, unless those points fall exactly halfway between two beads). In the classical limit

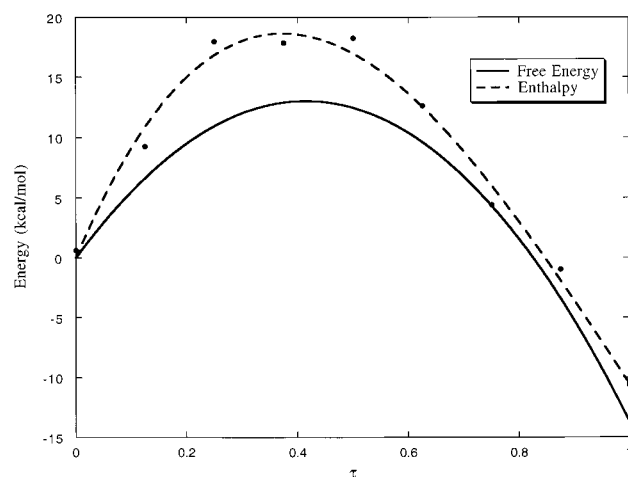


Figure 2. The change in free energy (solid line) and in energy (dashed line) as the partition function is changed from the initial to the final electronic state, i.e., as a function of τ . Both curves are cubic fits based on classical simulation results. The dots are the actual simulated energy values.

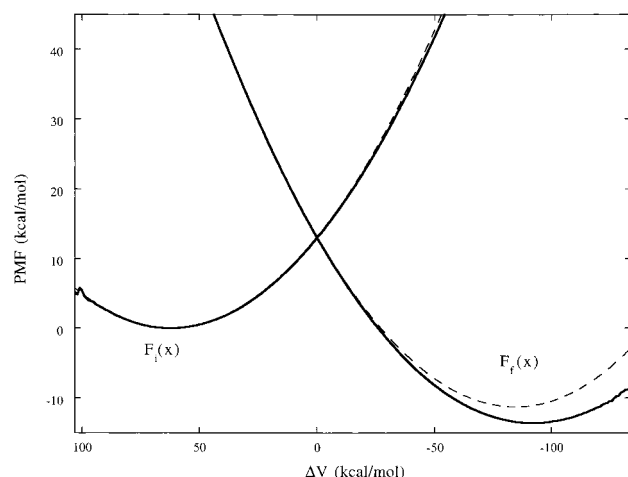


Figure 3. The potential of mean force (PMF) or free energy constrained along the reaction coordinate, ΔV , from the classical simulations. Quadratic curves (dashed) fit to the bottom of the initial-state well also are shown. The PMFs are very nearly harmonic and yield reaction and activation free energies that are close to the unconstrained values.

the exponents of the hybrid density operator commute, and there is a single bead in the interpolated potential $V_\tau = (1 - \tau)V_i + \tau V_f$.

B. Molecular Dynamics Simulations. The free energies were obtained from molecular dynamics simulations. The details of the potentials used will be discussed in section III, but a few aspects of the simulation methods should be mentioned as well. Both classical simulations and quantum path integral simulations were conducted. In both cases simulations were run at nine points between the initial and final states, $\tau = n/8$, $n = 0 \dots 8$. All systems were equilibrated for a few hundred picoseconds, and in each set of runs data was gathered for a total of 2.0 ns in the classical canonical simulations and 200 ps in quantum simulations and in classical microcanonical simulations. A RRESPA³² velocity Verlet algorithm was used with a long timestep of 1 fs for electrostatic, van der Waals, and dihedral interactions and a short timestep of 0.25 fs (in classical simulations) or 0.0625 fs (in quantum simulations) for the other potential interactions.

The two-time correlation functions discussed in section IV B were obtained from classical simulations run in a microcanonical ensemble (no thermostating) because dynamical infor-

mation is rigorously valid only in such simulations. A canonical ensemble was used for all other results because careful thermostating is necessary to obtain the entropy and free energy differences (section IV A). In the thermostatted runs a single four-link Nosé–Hoover chain was coupled to all the system and bath coordinates. A new noniterative Nosé–Hoover algorithm, described in Appendix A, was used. The target temperature in all simulations was 300 K, but the average temperature in thermostatted simulations was consistently 298 K. In the quantum simulations the bead velocities relative to their centroid velocities were resampled periodically (Anderson thermostating)³³ to ensure ergodicity: every 10 fs all bead velocities of a randomly selected quantized atom were resampled. The angle-dependent potentials of mean force (section IV E) were obtained in separate simulations using the program CHARMM24³⁴ with a single 0.5 fs timestep and a single Nosé–Hoover variable.

Although quantum imaginary-time correlation functions such as the one in eq 8 can be calculated directly from molecular dynamics simulation results, if the simulations are conducted in a canonical ensemble, the error range of such fluctuations is substantially greater than the error of averages such as that in eq 7. Thus in this paper only the average $\langle \Delta V \rangle_\tau$ was calculated directly from the simulation results. The integrals and derivatives of $\langle \Delta V \rangle_\tau$ were obtained numerically. Specifically, the average as a function of τ was fit to a quadratic polynomial form using linear regression, and the integrals, derivatives, and roots of the function were found analytically. Hence $F(\tau)$ was fit to a cubic polynomial. Results of direct numerical methods (e.g., trapezoidal integration), however, did not differ significantly. Other results, such as entropy differences, also can be obtained from either averages or fluctuations; in all cases the averages were used.

C. Electronic Structure Calculations and the Nonadiabatic Coupling. Electronic structure calculations were carried out using the spectroscopic version of the semiempirical INDO/s method developed by Zerner and co-workers.^{35,36} This method has been successfully applied to a broad range of organic, organometallic, and inorganic systems,^{37–39} and in particular it has been shown to be quite useful in evaluating donor/acceptor (D/A) coupling elements (V_{if}) for redox processes involving transition metal complexes.

The calculations were performed for the $(\text{Ru-pro}_4\text{-Co})^{3+}$ clusters in several conformations, and in some cases explicit waters of solvation were included in the quantum chemical calculations. In all cases the structures were based on the computer simulations. The effective point atomic charges included in the force field were taken from the INDO/s atomic populations for the initial and final states of the redox process (i.e., respectively, $(\text{bpy}')^-(\text{Co}^{3+})$ and $(\text{bpy}')(\text{Co}^{2+})$, where the donated electron initially is mostly on the bipyridine derivative (bpy') connecting the Ru and the first proline).

Estimates of V_{if} were obtained for transition-state structures by analyzing INDO/s results through use of the generalized Mulliken Hush (GMH) model.¹⁴ At the two-state GMH level, we have

$$V_{if}^d = \frac{|\vec{\mu}_{if}^d|}{|\Delta\vec{\mu}^d|} \Delta E^a \quad (10)$$

$$|\Delta\vec{\mu}^d| = (|\Delta\vec{\mu}^a|^2 + 4|\vec{\mu}_{if}^a|^2)^{1/2} \quad (11)$$

where the superscripts d and a denote, respectively, diabatic and adiabatic state properties, $|\Delta\vec{\mu}^a|$ ($|\Delta\vec{\mu}^d|$) is the magnitude of the adiabatic (diabatic) dipole moment difference, $|\vec{\mu}_{if}^a|$ is the

projection of the adiabatic transition moment along the $\Delta\vec{\mu}^a$ vector, and ΔE^a is the adiabatic vertical energy gap. Equations 10 and 11 show that V_{if} can be evaluated entirely in terms of adiabatic state properties. It is also important to emphasize that the GMH method may be applied to a system in an arbitrary configuration, thus eliminating the need to seek special points on the system potential energy surface (e.g., the transition state). Finally, eq 11 suggests a natural definition of effective donor–acceptor separation

$$r_{DA} = |\Delta\vec{\mu}^d|/e \quad (12)$$

where e is the magnitude of the electronic charge. The quantity r_{DA} may be interpreted as the distance separating the centroids of the effective donor and acceptor orbitals of the redox system.¹⁴

Cast as it is in terms of the transition moment, the GMH analysis applies to the vertical optical electron transfer process, which is the counterpart of the corresponding thermal process. To the extent that the Condon approximation is obeyed, similar magnitudes of V_{if} would be expected for the thermal process (occurring at the transition state) and the optical process (generally based on the equilibrium structure).

In its two-state INDO/s implementation, the GMH adiabatic states were taken as the configuration interaction (CI) eigenvectors corresponding to the initial and final charge states in the process of interest. The CI was based on self-consistent field (SCF) molecular orbitals (MOs) for the electronic configuration in which the Co site is in its low-spin (doublet) reduced form ((bpy')(Co²⁺)). The corresponding CI state was dominated by this SCF configuration ($\geq 95\%$ contribution), while the CI state forming the complement of the GMH two-state space is dominated ($\geq 90\%$) by a configuration of the (bpy')(Co³⁺). Despite the dominant role of these two configurations in the CI states, it was generally found that the major contributions to $\vec{\mu}_{tr}$ (and hence to V_{if} via eq 10) come from other configurations in the CI expansion. Attention is confined to the low-spin Co²⁺ state because this is most likely to be the primary product in the reduction process, as noted above.

The sensitivity of calculated V_{if} values was tested by variation of the active CI space and by adding a variable external potential. The active space included the highest n occupied and lowest n unoccupied SCF MOs where $n \leq 30$. In most cases, calculations were performed for $n = 25$ and $n = 30$. While the GMH method can be applied to a system at an arbitrary position along the reaction coordinate (see above), it was found convenient to bring the initial and final states (which were calculated for the most part in the absence of solvent) closer into resonance by adding an external potential based on point charges placed on the periphery of the DSA system along the Ru–Co axis. This potential lowered the energy of the (bpy')(Co³⁺) state relative to the (bpy')(Co²⁺) state. Energy lowerings of 2–4 eV (achieved with point charges of ± 0.75 – $1.5e$ 10 Å outside the Ru and Co atoms, respectively) were imposed in calculating the V_{if} results reported below.

III. Model

The simulated DSA system, which was fully described in the Introduction, bears a net charge of +3, arising from the charges of the Ru²⁺ and Co³⁺ sites, the negative charge of the carboxylate group linking the C-terminus proline to the Co acceptor, and the transferring electron. The equilibrium configuration of this system is extended (polypyrrole II), with ψ and ω angles averaging roughly 165° and 180°, respectively.

The DSA system is shown in Figure 1. In the simulations it is immersed in water. The electron transfer occurs primarily not from the Ru but from the attached bpy' anion; the transfer is to the OCo(NH₃)₅ group, yielding the reduced Co²⁺ in a low-spin (doublet) state as discussed above. The subsequent intersystem crossing^{15,40} to the high-spin state will not be considered in this paper.

The potential energy surfaces for the system are in a standard molecular mechanics form. The local interactions include harmonic bonds and Urey–Bradley terms (r), angles (θ), improper torsions (ω), and sinusoidal torsions (ϕ). The long-range interactions include Lennard–Jones van der Waals potentials and electrostatic potentials between atomic partial charges (q).³⁴ There also is a constant energy offset (\mathcal{E}) between the two potentials

$$V = \sum k_r(r - r_0)^2 + \sum k_\theta(\theta - \theta_0)^2 + \sum k_\omega(\omega - \omega_0)^2 + \sum [k_\phi - k_\phi \cos(n\phi - \phi_0)] + \sum \left(\frac{A_{ij}}{r_{ij}^{12}} - \frac{B_{ij}}{r_{ij}^6} \right) + \sum \frac{q_i q_j}{r_{ij}} + \mathcal{E} \quad (13)$$

The initial and final potentials, V_i and V_f , have different values of some of the parameters. There are hundreds of parameters that need to be specified. Parameters for the prolines and for the water (using the TIP3P flexible potential) were taken from the CHARMM22 all-atom potential.³⁴ The rest of the parameters were determined using experimental data, semiempirical electronic structure calculations, and analogy to other CHARMM parameters. Details follow, and the parameters are listed in Tables 1 and 2. Note that these parameters do not in general have physical significance other than determining the potential energy surfaces. Only simulation results (e.g., average coordinates, vibrational frequencies, and kinetic parameters) can meaningfully be compared with experimental data.

Partial Charges. The partial charges on the donor and acceptor groups are Mulliken populations derived from the INDO/s semiempirical electronic structure calculations described in section II C. The charges were averaged over equivalent or near-equivalent groups (the amine and pyridine groups), and charges on the transition metals were adjusted so as to yield integral charges (+1 or +2) for the donor ((bpy)₂Ru(bpy')) and acceptor (OCo(NH₃)₅) moieties. The procedure was carried out in both the initial and final electronic states, but the changes in charges on the bpy (but not bpy') Cs and Hs were found to be small and were neglected. The resultant partial charges are given in Table 1.

These partial charges model the transfer of a full electronic charge that initially is delocalized primarily ($\sim 80\%$) over the bpy' group between the Ru atom and the peptide and ultimately is delocalized over the pentaamminecobalt acceptor. Although they have not been rigorously derived and tested in conjunction with the CHARMM potential, they should be of sufficient accuracy to model the long-range solvation effects. Errors introduced into local interactions are partially compensated by fitting the other potential parameters.^{41,42}

Lennard–Jones Parameters. As the Lennard–Jones parameters are difficult to determine independent of the other parameters, they were taken from analogous parameters in the CHARMM potential: Zn for Co and Ru and similar atomic types of the same element for the C, N, and H atoms.

Bonds, Angles, and Torsions. Where possible, parameters were taken from similar small compounds in the CHARMM parameter set (benzene for pyridine and methylammonium for amine). The bipyridine C–N bond lengths were adjusted to

TABLE 1: Atomic Partial Charges Added to the CHARMM Parameter Set

	initial	final ^a
Ru	0.94 <i>e</i>	0.92 <i>e</i>
Bipyridine ^b		
N ₁	-0.36	-0.31
C ₂	0.11	
C ₃	-0.04	
C ₄	0.01	
C ₅	-0.04	
C ₆	0.05	
H ₃₋₆	0.10	
Bipyridine Derivative ^b		
N ₁	-0.39	-0.31
C ₂	0.07	0.11
C ₃	-0.10	-0.04
C ₄	0.03	0.11
C ₅	-0.09	-0.04
C ₆	0.04	0.05
H _{3,H5,H6}	0.07	0.10
C _m	-0.27	
H _m	0.09	
C	0.51	
O	-0.51	
Acceptor ^c		
Co	1.20	1.00
N	-0.39	-0.46
H	0.21	0.18
C	0.58	
O	-0.58	
O _t	-0.40	

^a Where final charges are left blank they are unchanged. ^b The two pyridines in each 2,2'-bipyridine are constrained to have the same charges. In each pyridine the heavy atoms are numbered sequentially. The N₁s are bound to the Ru, and the two pyridines in each bipyridine are linked at the C₂ positions. The H's are bound to C atoms with the same index. In the bipyridine derivative, bpy', the C_m and H_ms are in the methyl group (attached to one of the C₄s), and the CO group connects the other C₄ to the first proline. ^c The terminal-Co(NH₃)₅ is linked to the fourth proline carbonyl group by oxygen atom O_t.

literature values. The bond lengths and force constants for the metal-ligand bonds were selected to match classical simulation results with experimental data. Most of the equilibrium bond lengths were taken from crystal structures of the donor⁴³ and acceptor⁴⁴ groups. The vibrational frequencies for the metal-ligand bonds were mostly obtained from Raman spectra.⁴⁵ For the excited low-spin Co(II) state the Co-N and Co-O equilibrium lengths and frequencies had to be estimated on the basis of experimental data.^{25,30} Simulations with the fitted parameters yielded mean Co-N bond lengths of 1.97 and 2.09 Å, and frequencies of 491 and 383 cm⁻¹, respectively, for the Co³⁺ and low-spin Co²⁺ oxidation states, in comparison with the corresponding literature values^{24,25,30,45} (1.97 Å, 2.09 Å, 490 cm⁻¹, and 390 cm⁻¹). The same "force constant" parameters and same bond length change were used for Co-O as for Co-N.

Energy Offset. The overall energy offset between the two potential energy surfaces is due mostly to vacuum electronic energy differences. This offset was determined by matching the simulated reaction free energy to the best available estimate from experiment. A value of $\Delta F^\circ = F(1) - F(0) = -0.6$ eV (-13.84 kcal/mol) was used, close to the difference between the experimental redox potentials for the Ru^{2+/1+} couple (-1.2 eV)²¹ and the low-spin Co^{3+/2+} couple (-0.5 eV).^{28,29} As noted below, when comparing classical and quantum simulations the offset was fixed to match the quantum calculations; otherwise, the offset was determined separately for each set of simulations.

TABLE 2: Local Interaction Parameters Added to the CHARMM Parameter Set^a

	Bonds			
	initial		final ^b	
	<i>r</i> ₀	<i>k</i> _r	<i>r</i> ₀	<i>k</i> _r
Ru-N	2.04	95		
C-N	1.33	305		
C-C _m	1.49	250		
Co-N	2.05	175	2.22	110
Co-O	1.93	175	2.09	110
	Angles		Urey-Bradley terms	
	initial and final		initial	final ^b
	θ_0	<i>k</i> _θ	<i>r</i> ₀	<i>k</i> _r
Ru-N-C	120.0	30	2.99	22
N-Ru-N	90.0	50		
N-C-C	120.0	40	2.37	35
N-C-H	120.0	30	2.11	22
C-N-C	120.0	40	2.32	35
Co-N-H	109.5	44		
Co-O-C	109.6	40	2.97	30
N-Co-N	90.0	60		
N-Co-O	90.0	60		

^a Values are *not* in general the equilibrium values obtained from simulation. Units are Å (*r*₀), degrees (θ_0), kcal/mol/Å² (*k*_r), and kcal/mol/rad² (*k*_θ). ^b Where final parameters are left blank they are unchanged.

TABLE 3: Rate Constant and Kinetic Parameters from Classical Simulation and from Harmonic Models^a

	ΔF^\ddagger	$-d^2F/d\tau^2 _{ts}/2$	τ_{ts}	\bar{k}
classical simulation (anharmonic)	12.93	76.5	0.414	1.0
shifted frequency harmonic model	12.64	75.0	0.413	1.6
simply displaced harmonic model	12.32	74.4	0.407	2.8

^a The activation free energy (kcal/mol), free energy curvature (kcal/mol), dimensionless imaginary time at the transition state, and relative electron-transfer rate constant (normalized to the classical simulation result). $\Delta F^\circ = 13.84$ kcal/mol in all cases.

The DSA system contains 143 atoms; in the simulations it is solvated by 1097 water molecules in a 43 × 28 × 27 Å box. Periodic boundary conditions were used with long-range forces cut off using a group-based switched cutoff between 8 and 12 Å, except in the CHARMM simulations, which used the default atom-based cutoffs. In quantum simulations only the acceptor (OCo(NH₃)₅) was quantized; each quantum atom had 16 beads. For quantized atoms the cutoffs were based on the centroids; the consequent coupling between the different bead potentials is not expected to be significant.

IV. Molecular Dynamics Simulation Results

A. Classical Barrier and Reorganization. 1. Free Energies. The τ -dependent free energy from classical simulations is shown in Figure 2 (solid line). The transition state, where the free energy peaks, is at $\tau_{ts} = 0.4140 \pm 0.0005$; by symmetry it would equal 1/2 for electron transfer between equivalent sites. The system is significantly nonsymmetrical but is well within the Marcus normal region. The activation free energy is $\Delta F^\ddagger = F(\tau_{ts}) - F(0) = 12.93 \pm 0.03$ kcal/mol = 0.56 eV. The second derivative of the free energy, analogous to the reorganization free energy (λ) in the Marcus electron-transfer rate expression (eq 3), is $-d^2F/d\tau^2|_{ts}/2 = 76.46 \pm 0.09$ kcal/mol. These energies are tabulated in Table 3. The errors given here are purely statistical standard errors due to the finite length of the simulations. Errors in the simulated values of $\langle \Delta V \rangle_\tau$ of 0.12–0.16 kcal/mol are estimated from the correlation times and the

simulation lengths. The above errors in the kinetic parameters are then obtained from the covariances of the fitting parameters. Note that an estimated error of 0.05 kcal/mol in the simulated ΔF° , which is then adjusted to obtain ϵ , is not included in these errors.

The free energies $F(\tau)$ in the last paragraph are *not* constrained along any nuclear coordinate; they reflect the partition functions in different potentials interpolated between V_i and V_f . More traditional free energies used in the Marcus relation for the nonadiabatic transfer would be the free energy changes constrained along the electron-transfer coordinate ($\hat{x} = \Delta V$)

$$F(x) = -\frac{1}{\beta} \ln[P(x)] = -\frac{1}{\beta} \ln[\langle \delta(\hat{x} - x) \rangle] \quad (14)$$

where $P(x)$ is the population density (proportional to the constrained partition function) at coordinate $\hat{x} = x$. The constrained free energy is also called a potential of mean force. The constrained and unconstrained free energy differences between the reactant, transition state, and product are generally assumed to be the same, but this assumption is rarely tested quantitatively (they *are* the same for classical systems with parabolic PMFs). The constrained free energies are plotted in Figure 3. The results from simulations at different τ values were combined using the weighted histogram analysis method (WHAM).⁴⁶ The constrained reaction free energy, the difference between the minima of the two wells (based on a cubic fit), is $F_f(x_f) - F_i(x_i) = -13.81$ kcal/mol, compared to the unconstrained $\Delta F^\circ = -13.84$. The activation free energy, from the minimum of the initial state to the curve crossing, is $F_i(0) - F_i(x_i) = 12.92$ kcal/mol. The reorganization free energy, the difference along one curve between the minima of the two wells, is $\lambda_f = F_f(x_i) - F_f(x_f) = 75.8$ kcal/mol in the final state and $\lambda_i = F_i(x_f) - F_i(x_i) = 79.2$ in the initial state, for a mean value of 77.5. All of these values are very close to the unconstrained free energies given above. We also can check directly if the PMF curves are parabolic: in Figure 3 quadratic curves fit to the bottom of the initial-state well ($F_i(x) \lesssim 5$ kcal/mol) are shown.

2. Energies and Entropies. One can separate energetic from entropic contributions to the free energy by calculating the corresponding τ -dependent average energy. Besides its intrinsic interest, this separation is necessary in order to make comparison with the results of Arrhenius analysis of experimental data, which yield activation energies, not free energies. We refer to the energy rather than the enthalpy because the simulations were done at constant volume rather than at constant pressure. This distinction and the corresponding distinction between the Helmholtz and Gibbs free energy are, however, expected to be of minor quantitative significance. The energy is simply the average of the Hamiltonian, or for a classical system the average of the potential energy

$$E(\tau) \equiv -\frac{\partial}{\partial \beta} \ln Z(\tau) = \langle H_i \rangle_\tau \quad (15)$$

Thus, calculating the τ -dependent energy from simulation results is in principle trivial; in practice, large fluctuations in the energies require collecting data for long periods in order to control the error.

The τ -dependent average energies are shown with the free energies in Figure 2; the dots are simulated data, and the dashed line is a cubic fit. The reaction energy is $\Delta E^\circ = -10.8 \pm 1.6$ kcal/mol, and the activation energy is $\Delta E^\ddagger = 18.4 \pm 1.4$ kcal/mol, based on τ_{is} obtained from $F(\tau)$; the peak of $E(\tau)$ is

somewhat displaced at $\tau = 0.373$. The final state reorganization energy, $\langle H_f \rangle_i - \langle H_f \rangle_f = 72.8$ kcal/mol (the corresponding difference in initial-state energies is 81.6). Another measure of the reorganization energy, $-d^2E/d\tau^2|_{is}/2 = 104 \pm 6$ kcal/mol, is significantly larger. The curvature, however, is highly dependent on τ , varying from 179 to -1 kcal/mol as τ goes from 0 to 1 (with statistical uncertainties of roughly 25 kcal/mol and possible systematic error in the fit as well as in the model). Note that the reorganization energy in this paper is distinguished from the reorganization free energy. The entropy changes can be determined from $\Delta S = (\Delta E - \Delta F)/T$.⁴⁷⁻⁴⁹ The reaction entropy is $\Delta S^\circ = 10 \pm 5$ e.u. (cal/K·mol), and the activation entropy is $\Delta S^\ddagger = 18 \pm 5$ e.u. The reorganization entropy will be discussed below. Because the energy fluctuations are large, the statistical error of the simulated average energies is 1.1 to 1.4 kcal/mol, corresponding to error in the entropy of about 4 e.u.; after fitting, the errors of the energy differences above correspond to about 5 e.u. Even with the uncertainty, the entropy changes make a significant contribution to the free energy, as is apparent in Figure 2. The simulated results are compared with experimental results in section VI.

The DSA system contribution to the entropy change can be distinguished from the solvent contribution using a classical simulation of the system without solvent, which yields a reaction entropy of 3.8 e.u. Almost all of this system entropy change can in turn be attributed to a few acceptor modes using a simple harmonic model (denoted below as a "limited harmonic model"). The change in entropy of a classical harmonic mode depends on the change in frequencies: $\Delta S_{cl}^\circ = k_b \ln(\omega_i/\omega_f)$. The most significant frequency changes in our model are in the Co–N and Co–O stretches and in the H–N–H bends in the acceptor (see section IV B below). Using the model frequencies of 491 and 383 cm^{-1} for the Co–N and Co–O stretches yields a reaction entropy for only these six modes of 3.0 e.u., and frequencies of 1514 and 1483 cm^{-1} (from the spectral density described in section IV B) for the 15 H–N–H bends yield an additional 0.6 e.u. The rest of the entropy change, roughly 6 e.u., is due to the solvent and is dominated by the increase in entropy attending the reduction of the tightly solvated Co^{3+} . Detailed continuum calculations based on the charges given in Table 1 and a system cavity of realistic shape (analogous to those described in section VI) indicate that the entropy increase at the acceptor site is offset by an entropy reduction about half as large at the bpy' donor site (similar results are found for the changes in solvation free energy). The solvent entropy changes at the two sites reflect the difference in solvation due to the variation in the degree of charge delocalization and access to solvent at the two sites.

3. Nonparabolic Behavior and the Reorganization Entropy. The classical simulation results at 298 K are only partly compatible with the assumptions of Marcus theory.^{1,2} The free energy curves ($F(\tau)$ and $F(x)$) are nearly parabolic (Figures 2 and 3), with curvature of the $F(\tau)$ fit ranging only from 74 kcal/mol at $\tau = 0$ to 81 kcal/mol at $\tau = 1$. Furthermore, the Marcus expression, eq 4, together with the simulated ΔF^\ddagger value (12.93 kcal/mol) and the imposed ΔF° value (-13.84 kcal/mol) implies a reorganization free energy of 76.9 kcal/mol, very close to all of the simulated values given earlier in this section. The corresponding energy curves, however, are decidedly nonparabolic, as described above. Since $F = E - TS$, a nonparabolic energy implies a nonparabolic entropy $S(\tau) = \partial F(\tau)/\partial T$ and hence implies a corresponding departure of the free energy from near parabolic behavior as the temperature departs from 298 K. To be more precise, the above values imply a change with

each degree K of roughly 0.6 kcal/mol in the difference between the free energy curvatures at $\tau = 0$ and $\tau = 1$ (in the temperature range for which $S(\tau)$ remains unchanged). The pronounced nonparabolic behavior of $E(\tau)$ explains the large difference between estimates for the reorganization energy given above: 104 kcal/mol based on $-d^2E/d\tau^2|_{\text{ts}}/2$ vs 72.8 kcal/mol and 81.6 kcal/mol based on average energy differences for final and initial states, respectively.

More insight into the departure from Marcus behavior can be obtained by considering expressions for ΔE^\ddagger and for ΔS^\ddagger analogous to eq 4. Taking the temperature derivative of eq 4 yields (see also refs 19 and 50)

$$\Delta E^\ddagger = \frac{\partial(\beta\Delta F^\ddagger)}{\partial\beta} = \frac{1+\alpha}{2}\Delta E^\circ + \frac{1-\alpha^2}{4}\Delta E_\lambda \quad (16)$$

$$\Delta S^\ddagger = \frac{\partial\Delta F^\ddagger}{\partial\beta} = \frac{1+\alpha}{2}\Delta S^\circ + \frac{1-\alpha^2}{4}\Delta S_\lambda \quad (17)$$

where $\alpha = \Delta F^\circ/\lambda$ and ΔE_λ and ΔS_λ are, respectively, the reorganization energy and entropy. Equation 17 with the values for ΔE^\ddagger and ΔE° from the previous subsection and with $\alpha = -13.84/76.46$ would suggest an estimate for the reorganization energy $\Delta E_\lambda = 94.2$ kcal/mol. The departure of $E(\tau)$ from the parabolic form strongly suggests that neither the energy curvature at the transition state nor the value from eq 17, both based on parabolic models, is a reliable estimate of the reorganization energy. We adopt the mean value of the average energy differences, 77.2 kcal/mol, as a more accurate measure of ΔE_λ . This value is very close to the estimated λ (76.5 kcal/mol).

The reorganization entropy is a measure of the temperature dependence of the reorganization free energy. Often ΔS_λ is assumed to be negligible, but molecular-level studies of model electron-transfer systems using the mean spherical approximation (MSA) have yielded finite positive estimates of ΔS_λ for aqueous solvents.^{17,18} On the basis of the above best estimate of the reorganization energy, we conclude that the evidence is against any appreciable reorganization entropy in the simulated system. If one instead used the alternative reorganization energy estimates described above, one would obtain nonzero estimates of the reorganization entropy: 93 e.u. from $-d^2S/d\tau^2|_{\text{ts}}/2$ and 58 e.u. from eq 17. We note that the expected relation from eq 17, neglecting ΔS_λ , $\Delta S^\ddagger = \Delta S^\circ(1 + \alpha)/2 < \Delta S^\circ$ is not obeyed by the simulated entropy values, but we already have explained this apparent anomaly by concluding that the Marcus model is not applicable to the simulated entropies.

B. Solute and Solvent Dynamics. The nuclear motions associated with the electron transfer can be frequency resolved using the equilibrium two-time correlation function of the difference potential (the electron-transfer coordinate). The Fourier transform of this quantity, the spectral density (defined here without multiplying by the frequency), is shown in Figure 4 as calculated in the initial electronic state ($\tau = 0$), in a state near the transition state ($\tau = 3/8$), and in the final state ($\tau = 1$)

$$C_\tau(\omega) = 2 \int_0^\infty dt W(t) \cos(\omega t) (\langle \Delta V(t) \Delta V(0) \rangle_\tau - \langle \Delta V \rangle_\tau^2) \quad (18)$$

where $\langle \Delta V(t) \Delta V \rangle_\tau$ is the classical real-time correlation function for equilibrium in the potential V_τ and $W(t)$ is the three-term minimum Blackman–Harris window function.⁵¹ Note that the interpolated potential can be used instead of the hybrid density operator since the time-dependent correlation function can be calculated only for the classical system.

Several specific motions can be identified by their frequencies. The large peak at 493 cm⁻¹ for the initial state, near 453 cm⁻¹

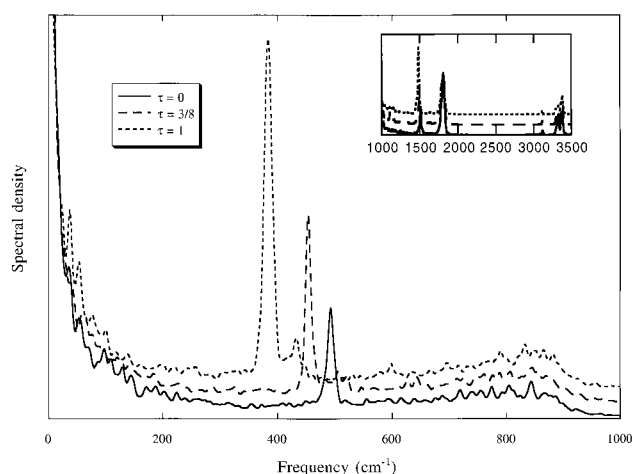


Figure 4. The spectral density (Fourier transform of the two-time correlation function) of the difference potential from classical simulations. The simulations were conducted in the initial electronic state (solid line), near the transition state (dashed line), and in the final state (dotted line). Small vertical offsets were applied for better visibility.

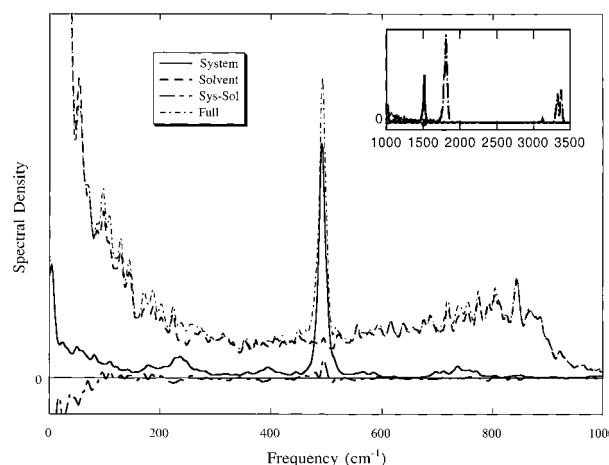


Figure 5. The spectral densities of the system–system (solid) and system–solvent (dashed) contributions to the difference potential compared to the overall spectral density (dotted) from classical simulations. The simulations were conducted in the initial electronic state ($\tau = 0$).

in the transition state, and at 384 cm⁻¹ in the final state is due to the Co–N stretch in the acceptor. The small peak near 1500 cm⁻¹ is due to the H–N–H bend in the acceptor amines. The peaks near 1810 cm⁻¹ are the water H–O–H bends. The H–O–H peaks and perhaps the H–N–H peak are likely spurious—in the electronically nonpolarizable, flexible water (amine) model the waters (amines) bend in order to adjust the monomer dipole moment in response to the transferred charge.⁵² At any rate, their contribution to the spectral density is not large. The peak at 3120 cm⁻¹ is the water O–H stretch.

Most of the motions contributing to the spectral density, however, occur in a broad band from 0–1000 cm⁻¹. These motions show little frequency change between the electronic states. Although it is difficult to distinguish specific atomic motions in this broad band, it can be separated into system and solvent contributions. Because the solvent–solvent interactions in our model are not affected by the electronic state, the difference potential ΔV contains only system–system and system–solvent components. The spectral densities of the two-time correlation functions of these components (in the initial state) are shown in Figure 5. Although system motions of many frequencies affect the difference potential, the influence of the

solvent is much stronger, particularly in the high-frequency region for which quantum effects (neglected here for now) should be significant. The cross-correlation function between the system and solvent components of ΔV is quite small.

C. Anharmonicity. The simulations use potential energy functions (eq 14) that include significant anharmonic contributions. In contrast, most quantum treatments of electron transfer assume a harmonic two-state (spin boson) model⁵³ in which the modes of the initial and final electronic states are displaced but are otherwise invariant; i.e., no frequency shifts or mode mixing accompany the electron-transfer process. We can test this model and examine anharmonic effects by constructing such a model (which we will call “simply displaced”) from our simulation results. For a simply displaced harmonic model, the difference potential is a linear function of the coordinates $\Delta V(\mathbf{x}) = -\sum K_n \Delta_n x_n + \Delta V(0)$, where K_n is the force constant and Δ_n is the displacement in mode x_n ; $\Delta V(0)$ is the potential difference at the arbitrary point where $\mathbf{x} = 0$. The classical spectral density of the difference potential is then (for $\omega > 0$)

$$C(\omega) = \frac{\pi}{\beta} \sum_n K_n \Delta_n^2 \delta(\omega - \omega_n) \quad (19)$$

Thus, from the simulated $C(\omega)$ we can obtain Δ_n (using mass-weighted coordinates). We can use the simulated $C(\omega)$ for any value of τ because, for model potentials that are only displaced, the model spectral density is the same for any V_τ . The results given here use data based on an interpolated potential near the transition state, $\tau = 3/8$.

For this simple model we can calculate (1) the exact nonadiabatic electron-transfer rate constant using eq 2 directly, (2) the stationary phase approximation to the rate constant (eq 5), and (3) the classical limit, which for this model reduces to the Marcus expression (eq 3). The expressions are given in Appendix C. The classical results are given in Table 3 (simply displaced harmonic model) and discussed here; quantum results will be discussed in the next section. The harmonic activation free energy is lower than the anharmonic simulation result by 0.6 kcal/mol, and the curvature is lower by 2.1 kcal/mol, corresponding to a rate enhancement by a factor of three. As there is no entropy change in this model, the activation energy (not shown) differs by considerably more (6.1 kcal/mol). The differences are due to anharmonicity of the simulation potential or to the enforced similarity of the initial and final state model potentials. Since the differences are relatively small, however, a carefully constructed harmonic model, such as the one just described, gives a reasonable approximation of the rate constant. Unfortunately, in many systems it may be difficult or impossible to obtain the spectral density in the transition state, which as defined here is a purely theoretical (albeit useful) construct. The spin boson model based on the initial-state spectral density gives an activation free energy that is 1.6 kcal/mol lower than the simulated barrier, or a rate constant high by a factor of 15. The differences in harmonic frequencies between the initial and transition states are as important as the anharmonicity. Hence, difficulty in obtaining parameters may cause as many problems for simple harmonic models as the potential form.

Frequency changes between the electronic states can be incorporated into a more complicated “shifted frequency” harmonic model that still can be treated analytically. In this model, each mode can have different frequencies in the initial and final electronic states and the minima can be displaced, but there still is no mixing of the modes (no Duschinsky rotation). For this model, $\Delta V = -\sum K_{f,n} \Delta_n x_n + \sum (K_{f,n} - K_{i,n})$

$x_n^2/2 + \Delta V(0)$ (taking $x_{i,n} = 0$), and the classical spectral density in the initial state is (for $\omega > 0$)

$$C_i(\omega) = \frac{\pi}{\beta} \sum_n \frac{K_{f,n}^2}{K_{i,n}} \Delta_n^2 \delta(\omega - \omega_{i,n}) + \frac{1}{2\beta} \left(\frac{K_{f,n}}{K_{i,n}} - 1 \right)^2 \delta(\omega - 2\omega_{i,n}) \quad (20)$$

where the force constants and frequencies now refer to one of the electronic states (i or f). Note that the PMF curves for this model (unlike the simply displaced harmonic model) are not in general parabolic.⁵⁴

Two spectral densities are needed in order to obtain the frequency shifts, but there is no general way of matching modes between the two spectral densities and, hence, in contrast to the simply displaced harmonic model, no unique mapping of the simulated spectral densities onto this model to obtain the parameters. Because of the similarity of the simulated spectral densities in the initial and final states (see Figure 4), we allowed frequency shifts only in six modes representing the Co–ligand stretches and 15 modes representing the H–N–H bends. The details of the procedure used to assign frequencies and displacements to these modes and additional constant-frequency modes are described in Appendix C.

The results for the shifted frequency harmonic model (Table 3) lie between those from simulation and those from the fixed-frequency harmonic model. The relevant equations are given in Appendix C. The classical activation free energy is 12.64 kcal/mol, 0.3 kcal/mol higher than in the spin boson model based on the transition state, but still 0.3 kcal/mol lower than the barrier in the simulated system. The curvature of the free energy is 75.0 kcal/mol, little changed from the spin boson model.

D. Quantum Effects. The effective electron-transfer barrier is generally lower than that found in classical simulations because of nuclear tunneling in high-frequency modes ($\hbar\omega \geq k_B T = 208 \text{ cm}^{-1}$) coupled to the electron transfer. Also, zero-point quantal effects can affect the reaction free energy. In our system significant nuclear tunneling is expected^{23–25} because of the Co–N stretches, in which there is a large displacement between the initial and final electronic states. Simulations in which the acceptor group ($\text{OCo}(\text{NH}_3)_5$) is quantized do show a somewhat lower barrier. Compared to the classical system with the same energy offset, the quantum activation free energy is 0.64 ± 0.09 kcal/mol smaller, and the reaction free energy is 1.29 ± 0.15 kcal/mol more negative (see Table 4). Note, however, that if the classical reaction free energy is adjusted to the experimental value (as in the results discussed above), the activation free energy is only 0.1 kcal/mol higher than the quantum result. Most of the quantum barrier suppression seems to be associated with change in the reaction free energy rather than in the reorganization free energy (see eq 4).

Using the limited harmonic model of specific modes introduced in section IV A2, we can attribute part of the quantum effects to particular motions of the acceptor. About one fourth of the change in the reaction free energy (-0.30 kcal/mol) can be attributed to the Co–N and Co–O stretches, and almost half (-0.49 kcal/mol) to the bends of the amine hydrogens, which are lighter and thus tunnel more easily. Additional frequency changes in the acceptor (not in our model) would cause added small quantum effects: using the same harmonic model of $\text{Co}(\text{NH}_3)_6$ as Richardson and Sharpe⁵⁵ yields a quantum shift of -2.2 kcal/mol in the reaction free energy.

TABLE 4: Quantum Effects on Rate Constant and Kinetic Parameters^a

	ΔF^\ddagger	$-\partial^2 F/\partial \tau^2 _{ts}/2$	τ_{ts}	\bar{k}
Simulations (Anharmonic)				
quantum (acceptor)	12.82	76.1	0.412	1.2
classical ^b	13.45	76.5	0.422	0.4
Shifted Frequency Harmonic Model				
quantum (full)	11.02	63.8	0.395	27.3 ^c
quantum (system)	12.34	73.0	0.409	2.7
classical ^b	12.97	75.0	0.418	0.9
Simply Displaced Harmonic Model				
quantum (full)	10.73	63.3	0.389	45.0 ^c
quantum (system)	12.04	72.4	0.404	4.6
classical	12.32	74.4	0.407	2.8

^a The activation free energy (kcal/mol), free energy curvature (kcal/mol), dimensionless imaginary time at the transition state, and relative electron-transfer rate constant (normalized to the classical simulation (anharmonic) result in Table 3). "Quantum" results in table use the stationary phase approximation (see text). The degree of quantization (acceptor only, DSA system only, or all modes) is noted parenthetically and described in the text. ^b Classical results are based on the same energy offset \mathcal{E} used in the corresponding quantum calculation and thus differ from those in the previous table. The classical reaction free energy is -12.55 kcal/mol for the simulation result and -13.06 for the shifted frequency harmonic model, compared to -13.84 for the quantum results. ^c Exact quantum results for the harmonic rate constants (to be compared to the stationary phase results in the table) are 32.0 (vs 31.9) for the shifted frequency harmonic model and 53.4 (vs 53.2) for the simply displaced harmonic model.

As noted earlier, the dominance of solvent contributions in most of the high-frequency region of the ΔV spectral density (see Figure 4) suggests that quantization of the solvent could be important for electron-transfer energetics. Bader, Kuharski, and Chandler¹⁰ found for the simpler aqueous ferrous–ferric system that solvent beyond the first solvation shell accounted for roughly half of the quantum suppression of the electron-transfer barrier.

Quantum effects due to the solvent and to DSA system modes outside the acceptor can be estimated from the harmonic models described in the previous section. In these models all of the modes coupled to the electron transfer can be quantized, including solvent modes. The reaction barrier results are included in Table 4. For the fixed-frequency model there is a 1.6 kcal/mol quantum decrease in the effective barrier (and owing to the potential form, no effect on the reaction free energy). In the shifted frequency model the quantum suppression is slightly larger, 1.9 kcal/mol, and the reaction free energy is 0.8 kcal/mol more negative than in the classical calculation. In both harmonic models the curvature of the free energy decreases roughly from 75 kcal/mol (classical) to 63 kcal/mol (quantum), and quantum effects increase the rate constant by a factor of 15 (fixed) and 29 (shifted). For comparison, harmonic models in which only the DSA system modes are quantized can be derived using the separate system and solvent correlation functions (they were renormalized slightly to match the full correlation function). With only the system modes quantized, the quantum effects are comparable to those in simulations with a quantized acceptor (see Table 4). Thus, most of the quantum suppression of the barrier in our system can be attributed to the broad band of solvent modes.

We also can test the stationary-phase ansatz for the harmonic models by comparing the exact calculation of the rate constant to the stationary-phase approximation. The rate constants differ for each of the harmonic models by less than 0.25%, which would correspond to an activation energy difference of about 1 cm⁻¹. Thus, for these models the stationary phase approximation

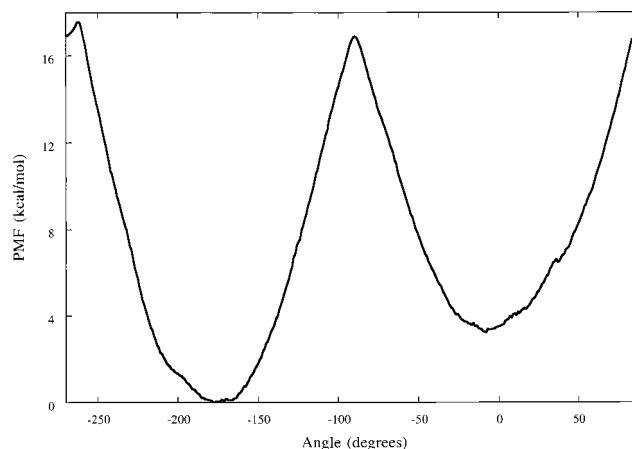


Figure 6. The potential of mean force (PMF) along the ω_3 dihedral angle associated with the bond linking the third and fourth proline amino acids. Results are from classical simulations for the initial electronic state ($\tau = 0$).

is excellent. Song and Marcus⁵⁶ found almost as good agreement for a spin boson model of another system based on an experimentally derived spectral density.

Quantization also affects the entropy changes. The entropy change in a quantum oscillator is smaller than that in a classical oscillator with the same frequencies because of the limited number of accessible vibrational states. In the selected acceptor modes discussed above, the quantum entropy change is 2.1 e.u. (rather than 3.0 classically) for the Co–ligand bonds and 0.0 (rather than 0.6) e.u. for the amine bends. Additional quantum effects could occur in the other modes, including solvent modes. Thus, the classical simulation results likely exaggerate somewhat the entropy changes in our model, although opposite contributions from the donor and acceptor sites may complicate the situation.

E. Conformers and Barriers. Experiments on polyproline systems have been used to explore the distance dependence of electron-transfer rates, with the assumption that chains of at least four prolines form rigid helices and thus that the distance over which the electron is transferred is proportional to the number of prolines.²¹ Others, however, suggested, on the basis of previous simulations, that the electron transfer occurs with the peptide bent because of rotation of some combination of ω and ψ backbone dihedral angles.²² The bent conformations have much shorter donor–acceptor distances (the Ru–Co distance in our simulations was roughly 14–16 Å with a bent backbone vs 19 Å in an extended polyproline II conformation), and hence were expected to show much larger electronic coupling. We investigated the conformational dependence of both the free energy and the electronic coupling. The former is described here; the latter will be discussed in section V.

The probability of the system achieving a particular nuclear conformation is examined using the potential of mean force constrained along an internal coordinate (for the classical, fully solvated system). The PMF was defined in eq 14, where x now indicates an internal angle. The free energy at barriers high compared to thermal populations can be obtained using umbrella sampling, in which a series of bias potentials are applied to the selected coordinate.³ The results were pieced together using WHAM.⁴⁶ In general, except for the constrained angles, the peptide remained in the extended (polyproline II) conformation.

The PMF for the ω_3 dihedral angle, $C_\alpha-C-N-C_\alpha$, between the third and fourth proline amino acids is shown in Figure 6. There are two wells, one near 180° (trans well) and one near 0° (cis well), with the cis well about 3 kcal/mol higher in energy.

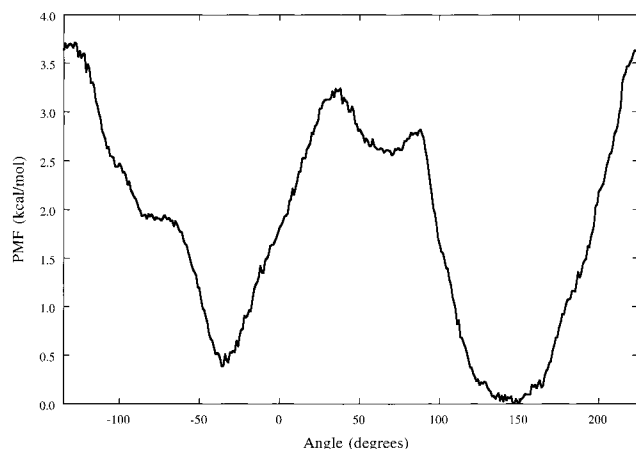


Figure 7. The potential of mean force (PMF) along the ψ_4 dihedral angle associated with the linkage of the fourth proline amino acid and the acceptor. Results are from classical simulations for the initial electronic state ($\tau = 0$).

The barrier between the two wells is about 17 kcal/mol. As the population is proportional to $\exp[-\beta F(x)]$, somewhat less than 1% of the equilibrium population should be in the cis well. The rate of crossing the barrier from trans to cis wells ($k_B T/h \exp[-\beta(F(x_{\text{cis}}) - F(x_{\text{trans}}))]$) is on the order of inverse seconds, thousands of times slower than the electron transfer.²¹ Thus, once the small initial population in the cis well has transferred to the final electronic state, no more population will reach the cis well.

Similar calculations (not shown) were done for the ω_1 angle between the first and second prolines and for the ψ_2 angle, N-C $_{\alpha}$ -C-N, between the second and third prolines (the angles were chosen on the basis of ref 22 and on minimization calculations that used Monte Carlo selection of backbone dihedral angles). Both PMF calculations yielded even higher barriers.

The PMF for the ψ_4 angle connecting the fourth proline to the acceptor, N-C $_{\alpha}$ -C-O, shown in Figure 7, looks quite different. The bent (α) conformation is only 0.5 kcal/mol higher than the extended (β) conformation, with a relatively small barrier of about 3 kcal/mol. This is perhaps the least well parametrized part of the model potential energy surface, as many of the parameters were obtained for proline and Co(NH₃)₆ separately, but, if the result is valid, all conformations of this angle appear to be accessible.

V. Electronic Coupling

Electronic coupling elements, V_{if} , calculated as described in section II C for selected peptide conformations of interest, are presented in Table V, along with the corresponding effective donor-acceptor separations, r_{DA} , as defined by eq 12 and the Ru-Co separations, r_{RuCo} . Since the transferring electron is strongly localized on the bpy' ligand, we find as expected that $r_{\text{DA}} < r_{\text{RuCo}}$.

For a given conformation, the calculated V_{if} magnitudes are rather sensitive to the details of the calculations. These details include the number of electronic configurations involved in the CI (as many as $\sim 10^3$ were included in the largest active spaces sampled) and the magnitude of an applied external field. This latter test of sensitivity may be viewed as a partial measure of the response of the coupling to the electrical fluctuations of the surrounding medium. For the case of $\psi_4 = -20^\circ$, comparative calculations with and without a sheath of water molecules indicated little influence of solvent on V_{if} magnitude.

TABLE 5: Calculated V_{if} Values as a Function of Backbone Conformation

conformation (deg)	coupling (cm ⁻¹)	effective D/A separation (Å) ^d		
ψ_4^a	ω_3^b	V_{if}^c	r_{DA}	r_{RuCo}
140.0 ^e	-178.0	~ 0.5 – 5.0	18.9	19.3
0.0	-178.0	~ 0.2	18.0	18.4
-20.0	-178.0	0.01–0.10 ^f	17.8	18.5
-40.0 ^g	-178.0	~ 0.1	17.7	18.6
-60.0	-178.0	~ 0.2	18.4	18.8
-70.0	-178.0	1–30	18.4	18.9
-20.0	-10.0 ^h	30–50	10.5	11.5

^a Torsion angle with respect to the bond linking the α carbon and the carbonyl carbon of the fourth proline moiety (i.e., that linked to the Co coordination complex). ^b Torsion angle with respect to the amide C-N bond linking the third and fourth proline moieties. The value -178.0° is near the lowest energy local minimum (see Figure 6).

^c Calculated on the basis of eq 10, as discussed in section II C, for the minimum energy transition state structure and selected conformational variants. The calculations employed an active space consisting of the highest 25–30 occupied and lowest 25–30 unoccupied MOs and did not include solvent molecules, except as noted in footnote f. To compensate partly for the absence of a polarized medium, the energy of the initial state (bpy⁻/Co³⁺) was lowered relative to the final state by the use of point charges. Shifts of 2–4 eV were considered in order to test the sensitivity of the calculated V_{if} values. This sensitivity, together with that associated with variation of the active CI space, is reflected in the V_{if} table entries. ^d The relationship $r_{\text{DA}} \sim r_{\text{RuCo}}$ reflects the strong localization of the donor orbital on the bpy' ligand; r_{DA} is defined in eq 12. ^e Near the lowest-energy local minimum (see Figure 7). ^f Analogous calculations employing a shell of 38 water molecules based on the simulation results yielded results in the same range. ^g Near the secondary local minimum with respect to ψ_4 (see Figure 7). ^h Near the secondary local minimum with respect to ψ_3 (see Figure 6).

Despite the noise level due to the sensitivity just discussed, pronounced systematic variation of V_{if} magnitude with peptide conformation is apparent. For the broad range of ψ_4 angles, this variation occurs even though r_{DA} remains effectively constant (~ 18 Å). It is of interest to note that one of the largest V_{if} magnitudes is in the vicinity of the lowest local minimum of the PMF curve shown in Figure 7. The V_{if} results will be discussed in the context of the available experimental data in the next section.

The variations of V_{if} obtained in this study offer interesting examples of departures from a simple model (in the framework of the Condon approximation) based on the use of a fixed electronic coupling parameter. Furthermore, r_{DA} by itself is seen not to be a reliable guide for estimating variations in V_{if} . The large variations in V_{if} suggest that electron transfer may occur from accessible nonequilibrium conformations of the DSA system.

VI. Comparison with Experiment

In order to make contact with the experimental kinetic data,²¹ it remains to correct the raw calculated quantities for certain deficiencies of the computational model and then to cast the results in a form corresponding as closely as possible to the phenomenological Arrhenius rate constant model^{20,21,57}

$$k = \frac{k_B T}{h} \exp(\Delta S^\ddagger/k_B) \exp(-\beta \Delta E^\ddagger) \quad (21)$$

where ΔE^\ddagger is the activation energy and where the effective "activation entropy" is assigned a "prime" to underscore the fact that it contains contributions from both the nonadiabatic prefactor (see eq 3) and the entropic component of ΔF^\ddagger .

A. Correction of the Calculated Solvent Reorganization Free Energy. The reorganization free energy for the process

under study, denoted as λ , is dominated by the solvent contribution, λ_s (in the simply displaced harmonic model λ is proportional to the integral over the spectral density shown in Figure 4). The calculated value of λ_s suffers from two defects of the potential model: the use of a finite cutoff for electrostatic interactions (see section III) and the use of an electronically nonpolarizable solvent model. These two effects are expected, respectively, to lead to an artificial reduction and exaggeration of λ_s , as can be seen from the reorganization free energy due to a charge shift in a single spherical cavity surrounded by a continuum dipolar solvent shell

$$\lambda_s = c \frac{\Delta q^2}{2} \left(\frac{1}{r} - \frac{1}{R} \right) \quad (22)$$

where Δq is the change in charge, r is the solute cavity radius, and R is the outer radius of the solvent shell (set to infinity for bulk solvation, but assigned a finite value to correspond to a simulation using a finite electrostatic cutoff (see section III). The Pekar factor⁵⁸ c is

$$c \equiv \frac{1}{\epsilon_\infty} - \frac{1}{\epsilon_0} \quad (23)$$

where ϵ_∞ and ϵ_0 are the optical and static dielectric constants. For a nonpolarizable solvent model, ϵ_∞ is nominally equal to unity, whereas for liquid water, $\epsilon_\infty = 1.8$.^{2,10,59}

We have chosen to correct the simulated λ value, taken as 76.5 kcal/mol (the classical simulation value for $-d^2F/d\tau^2|_{ts}/2$ given in Table 3) on the basis of the following procedure. The λ_s component of λ is identified as 60.8 kcal/mol, the difference between the total value and the value (15.7 kcal/mol) obtained from a classical simulation of the electron-transfer process for the isolated system. An alternative estimate of λ_s , using the solvent component of the spectral density and a simply displaced harmonic model, yielded a very similar value, 61.8 kcal/mol. The value of λ_s was corrected using a model with a continuum solvent and a realistic molecular solute cavity based on the superposition of the atomic spheres of all atoms of the system (as, for example, described in ref 60). (Such a procedure rests, of course, on the assumption of a fixed solute cavity serving both initial and final states in the electron-transfer process.⁶¹) Each system atomic sphere was assigned a point charge change $\Delta q \equiv q_f - q_i$ using the data displayed in Table 1. To mimic the finite cutoff used in the simulation, one continuum λ_s calculation was based on a sheath of aqueous solvent extending 10.1 Å beyond the solute cavity surface⁶² (the soft cutoff used in the simulations corresponds, for $1/r^2$ fields in a continuum solvent, to a hard cutoff of 10.1 Å). The resulting λ_s value, using the experimental ϵ_0 value for water (78) and the nonpolarizable model ϵ_∞ value (1.0), was found to be within 4% of the simulated value. This close correspondence between the simulated and continuum solvent energetics supports the use of the continuum model to correct the simulated results. We correct the simulation results for the polarizability of water by scaling⁶³ the nonpolarizable λ_s value (60.8) by the ratio of the Pekar factor c based on $\epsilon_\infty = 1.8$ and $\epsilon_\infty = 1$: $0.54/0.99 = 0.55$, as follows from eq 23. (A very similar ratio, 0.58, is obtained from the results of the detailed continuum calculations. Any moderate inaccuracy in ϵ_0 for the model water would make negligible difference to this calculation.) The difference between the continuum λ_s estimates for the finite solvent sheath and an infinite solvent environment (using $\epsilon_\infty = 1.8$), 5.7 kcal/mol, is taken as the value of the finite-size correction. Combining this

TABLE 6: Calculated Activation Parameters from Classical Simulation Results^a

	uncorrected ^b	corrected ^c
ΔF^\ddagger (kcal/mol)	12.9 ± 0.1	7.7 ± 0.1
ΔE^\ddagger (kcal/mol)	18.4 ± 1.5	13.2 ± 1.5
ΔS^\ddagger (e.u.)	18.3 ± 5.0	18.3 ± 5.0
λ (kcal/mol)	76.5 ± 0.1	54.8 ± 0.1
λ_s (kcal/mol)	60.8 ± 0.1	39.1 ± 0.1
α	-0.18	-0.25

^a Activation free energy (ΔF^\ddagger), energy (ΔE^\ddagger), and entropy (ΔS^\ddagger); the reorganization free energy (λ) and its solvent component (λ_s); and the ratio $\alpha \equiv \Delta F^\circ/\lambda$. Energy offset ϵ adjusted to give $\Delta F^\circ = -13.8$ kcal/mol, and $\Delta S^\circ = 10.5$ e.u., for both corrected and uncorrected results. Note that results do not include quantum effects, which, for example, are estimated to reduce ΔF^\ddagger by 1–2 kcal/mol. ^b Calculated with finite cutoff for intersite interactions and with nonpolarizable solvent model (see section III). ^c See section VI.

value with the scaled simulation result (33.4 kcal/mol) yields a final estimate of 39.1 kcal/mol for λ_s and 54.8 kcal/mol for λ .

B. Arrhenius Analysis. To reconcile eq 21 with eq 3 or eq 5 we must both correct ΔF^\ddagger using the adjusted reorganization free energy and remove its entropic component. As the classical simulation results are in close conformity with the Marcus activation free energy expression, eq 4, we use the corrected value of λ and the experimentally inferred (and hence uncorrected) value of ΔF° in that expression to obtain a corrected $\Delta F^\ddagger = 7.7$ kcal/mol, 40% smaller than the uncorrected result.

The classical simulation results, however, are *not* compatible with the corresponding Marcus relations for activation energy (eq 17) or entropy (eq 17), as discussed in section IV A3. Thus we cannot correct ΔS^\ddagger as we did ΔF^\ddagger . In section IV A3, however, we concluded that the preponderance of evidence from the classical simulations suggests a minor contribution from reorganization entropy. The apparent lack of a ΔS_λ contribution suggests that corrections to ΔS^\ddagger are likely to be rather minor (e.g., a modest finite-cutoff correction) and can be neglected. The simulated ΔS^\ddagger value (18 e.u.) together with the corrected ΔF^\ddagger value dictates the correction to be made in ΔE^\ddagger .

The initial and corrected activation parameters are summarized in Table 6. In view of the estimated quantum reduction of the classical activation barrier by ~ 1 –2 kcal/mol (Table 4),⁶⁴ the corrected classical value of ΔE^\ddagger (13.2 ± 1.5 kcal/mol)⁶⁵ is in reasonable accord with the experimentally inferred activation energy, 9.4 ± 0.2 kcal/mol,²¹ which would include such quantum effects. A more complete quantum treatment of all solvent modes using path integral simulation rather than a harmonic model might increase the quantum barrier suppression, thus bringing the simulated result to even closer agreement with the experiment.

Equating eq 3 and eq 21 yields the following relationship among ΔS^\ddagger , λ , V_{if} , and $\Delta S^{\ddagger'}$:

$$(k_B T) \exp(\Delta S^{\ddagger'}/k_B) = V_{if}^2 \left(\frac{4\pi^3}{k_B T \lambda} \right)^{1/2} \exp(\Delta S^\ddagger/k_B) \quad (24)$$

The calculated λ and ΔS^\ddagger values (corrected results, Table 6) together with the experimental $\Delta S^{\ddagger'}$ value²¹ (-5.5 e.u.) thus imply V_{if} in the range 0.2 – 2.0 cm^{-1} . In contrast, if ΔS^\ddagger were neglected, a considerably larger V_{if} value (~ 50 cm^{-1}) would be required to accommodate the experimental data. Calculated V_{if} values of roughly the correct magnitude (Table 5) are found for regions of the ψ_4 conformational space near the local minima of the PMF shown in Figure 7.

C. Experimental Estimates of the Reaction Entropy. Experiments with temperature-controlled electrochemical cells

have found sizable entropy changes in related systems. Hupp and Weaver¹⁶ estimate a reaction entropy of 45 e.u. for aqueous $\text{Co}^{3+/2+}(\text{NH}_3)_6$ (high-spin final state), of which Richardson and Sharpe⁶⁶ attribute 17.4 e.u. to intramolecular nuclear and electronic changes, thus implying a 28 e.u. contribution due to solvent. A smaller solvent contribution ($\lesssim 20$ e.u.) is indicated for the $\text{Ru}^{3+/2+}(\text{NH}_3)_6$ system,¹⁶ even though this couple would be expected to have solvation properties similar to those of $\text{Co}^{3+/2+}(\text{NH}_3)_6$ since both systems have the same charges and similar size. The entropy change for the electron transfer studied here is reduced relative to that for the high-spin $\text{Co}^{3+/2+}(\text{NH}_3)_6$ complex both because of the compensation at the donor site discussed above in section IV A2 and because one must exclude the entropy change for intersystem crossing from low-spin to high-spin Co(II). Neither is likely to account for all of the difference between the net value (10.6 e.u.) obtained in the present study and the somewhat larger value implied by the estimates based on experiment.^{16,66} The simulated intramolecular entropy change is low because not all frequency changes are well parametrized in the model; the solvent contribution to the entropy change is low in part because of the potential cutoffs.

VII. Conclusions

We have calculated the primary ingredients required for a complete kinetic analysis of the electron-transfer process in a model biological system: the activation free energy and electronic coupling results are summarized in Tables 3–6. Among the issues of major mechanistic interest are the importance of quantal effects and of anharmonicity on the activation energetics. Table 4 displays clear trends in both. (1) For a given potential model (anharmonic, harmonic with frequency shifts, or harmonic without frequency shifts), the activation barrier is lower and “earlier” (i.e., τ_{ts} closer to the initial state) and the associated reorganization free energy ($-d^2F/d\tau^2|_{\text{ts}}/2$) is smaller, as one proceeds from the fully classical system to a system with some quantized modes to a fully quantal system (including solvent). The quantal barrier suppression is primarily due to nuclear tunneling, with a substantial contribution from solvent modes (reflecting the coupling of high frequency solvent motions to the electron transfer), reaching 1.9 kcal/mol for a fully quantal harmonic model. In addition, simulations yield a quantal enhancement of the reaction exothermicity by 1.2 kcal/mol because of zero-point energies in a partially quantized system. (2) For a given level of quantization, the activation barrier becomes higher and later in proceeding from the fixed frequency harmonic to the shifted frequency harmonic to the anharmonic potential model. The harmonic models underestimate the reaction barrier (by up to 0.9 kcal/mol) because they underestimate the reorganization that occurs upon electron transfer.

These trends should not be affected by the limitations of the simulation model solvent, i.e., the cutoff of electrostatic forces and the lack of electronic polarizability. Correction for these defects, however, as well as correction for quantum solvent effects, is necessary for meaningful quantitative comparison with experiment. The cutoff decreases the free energy barrier, and the incorrect optical polarizability and the classical treatment of the solvent increase it. The net correction for the classical solvent model, using a continuum electrostatic model, is to decrease the simulated barrier by $\sim 40\%$. Quantizing the solvent in a harmonic model further suppresses the barrier by roughly 1.3 kcal/mol. It would be relatively straightforward, although computationally expensive, to avoid cutoffs by using Ewald sums (see, e.g., ref 67) and to quantize all the solvent.

Eliminating the largest correction, however, would require an electronically polarizable water model, a rather difficult problem for large-scale simulations.

The activation entropy (which in our best estimate is uncorrected) must be separated from the activation free energy in order to permit comparison with experimental Arrhenius analysis, which yields an activation enthalpy, not free energy. The corrected activation energy from simulations is quite close to the experimental result.

The electronic coupling must be combined with the activation entropy to compare with the experimental Arrhenius prefactor. This analysis requires an electronic coupling of $0.2\text{--}2\text{ cm}^{-1}$ in order to match experimental results. The calculated electronic coupling at the apparent equilibrium configuration of the system is within this range. As inclusion of solvent orbitals has little effect on the coupling, electron-transfer paths via the solvent molecules do not seem to contribute to the coupling.

The electronic coupling in other (nonequilibrium) nuclear configurations of the system can be an order of magnitude larger or smaller. Such couplings are irrelevant if the configurations are energetically inaccessible. Rotamers of selected backbone dihedral angles appear inaccessible on the time scale of electron transfer, not because of the rotamer free energies but because of the large barriers to rotation. Rotation of the acceptor relative to the polypeptide yields configurations that appear accessible and which also have substantial electronic coupling (especially near $\psi_4 = -70^\circ$). Although the barrier to electron transfer at these nonequilibrium configurations should be increased to account for the energy needed to reach them, electron transfer in these configurations could make a significant contribution to the overall rate. To quantify such contributions one would need to simulate the electron-transfer barrier while constraining the system to the nonequilibrium configurations. Dynamic effects of the configuration-dependent coupling also could alter the electron-transfer rate; such effects could be investigated using the approach described in Appendix B.

If electron transfer occurs from multiple nuclear configurations of the system, it could cause multiexponential or nonexponential kinetics of electron transfer. Small initial populations in backbone rotamers could yield small fast components, and simultaneous changes in the energetics and the coupling along the ψ_4 angle could complicate the basic kinetics. Such a departure from exponential kinetics would complicate the analysis of the rate constant as a function of the number of prolines in the spacer.²¹ In addition, a meaningful treatment of variation with number of prolines would require a more accurate evaluation of V_{if} than that reported in the present work. Examination of systems with different numbers of prolines using the molecular dynamics simulation methods described in this paper, however, could help elucidate the dependence on the spacer of the free energetics and of the stability of the polyproline-II structure.

Overall, we have demonstrated the ability to calculate nonadiabatic electron-transfer rate constants for a model biological system, including nuclear energetic and entropic and electronic contributions, but the molecular mechanical simulation models are not yet accurate enough to make the simulated rate constant quantitative without correction. (Fortunately, these corrections are of known origin and relatively standard.) Such simulations and calculations do, however, allow important detailed mechanistic investigations of the electron-transfer process, including distinguishing solvent contributions, quantum effects, anharmonic effects, and key nuclear configurations.

Acknowledgment. We thank Amir Karger, Dr. August Calhoun, Prof. Stephan Isied, Dr. Yeung Shin, Dr. James Wishart, and Dr. Roland Billing for helpful discussions. Most of the molecular dynamics simulations used a modified version of code by Amir Karger. This research was supported by a Camille Dreyfus Teacher–Scholar award to G.A.V. and by a University of Utah seed grant. The work at Brookhaven National Laboratory (MDN) was supported by the Division of Chemical Sciences, U.S. Department of Energy, under grant DE-AC02-98CH10886.

Appendix A: An Alternative Noniterative Nosé–Hoover Chain Algorithm

In Newtonian molecular dynamics simulations the total energy is constant, and thus time-averaging yields a microcanonical ensemble (in an ergodic system). Several methods have been used to simulate a canonical ensemble, with a Boltzmann distribution of energies for a chosen average temperature; one of the most effective of these is to couple the system to one or more Nosé–Hoover chains.^{68–70} As originally formulated for standard propagation algorithms, this method required iterative convergence of the equations of motion because the time derivative of each system or Nosé–Hoover velocity depends on the current value of the velocity. Recently, Jang and Voth⁷¹ have proposed several noniterative algorithms for Nosé–Hoover chains, all valid to second order in the dynamics timestep. This appendix describes a slightly different algorithm that was used in the present study.

In Nosé–Hoover chain dynamics, the equations of motion for the system variables (q_i , v_i) and the Nosé–Hoover variables (\bar{q}_η , \bar{v}_η) are

$$\begin{aligned}\dot{q}_i &= v_i \\ \dot{v}_i &= -a_i(\mathbf{q}) - \bar{v}_1 v_i \\ \dot{\bar{v}}_\eta &= \bar{a}_\eta(\bar{v}_{\eta-1}) - \bar{v}_{\eta+1} \bar{v}_\eta \\ \dot{\bar{q}}_\eta &= \bar{v}_\eta\end{aligned}\quad (\text{A1})$$

where $a_i = 1/m_i \partial V(\mathbf{q})/\partial q_i$, $\bar{a}_1 = (\sum_i m_i v_i^2 - Nk_B T)/\bar{m}_1$, and $\bar{a}_\eta = (\bar{m}_{\eta-1} \bar{v}_{\eta-1}^2 - k_B T)/\bar{m}_\eta$ for $\eta > 1$. N is the number of system degrees of freedom coupled to the chain, $\bar{v}_{M+1} = 0$ (where M is the number of Nosé–Hoover variables), T is the target temperature, m_i are the system masses, and \bar{m}_η are the Nosé–Hoover “masses.” In the leapfrog or velocity Verlet propagation algorithms the system positions and velocities are updated alternately. All of Jang and Voth’s algorithms are based on the division of the Nosé–Hoover variables into two sets: \bar{v}_{2k+1} and \bar{q}_{2k} are updated with the positions q_i , and \bar{v}_{2k} and \bar{q}_{2k+1} are updated with the velocities v_i . The time derivative of each variable in each set depends only on the variable itself and on the variables in the other set. Various approximations are made to yield simple algorithms valid to second order in the timestep.

In the new algorithm used here, the single approximation is made to hold the variables in the other set constant at their current known values. Then each propagation equation becomes a linear first-order differential equation that can be solved exactly. The general result for a single timestep δ is

$$\begin{aligned}q_x(t_q + \delta) &= q_x(t_q) + \delta v_x(t_q) \\ v_x(t_v + \delta) &= \exp[-\delta v_{x+1}(t'_q)] v_x(t_v) + \\ &\quad \delta a_x(t'_q) \frac{1 - \exp[-\delta v_{x+1}(t'_q)]}{\delta v_{x+1}(t'_q)}\end{aligned}\quad (\text{A2})$$

where x stands for either i (system variables) or η (Nosé–Hoover variables); for $x = i$, v_{x+1} is \bar{v}_1 . Here t_q (t'_q) are times at which q_x (a_x and v_{x+1}) are known; v_x is known at t_v . In the leapfrog algorithm these times will be at half timesteps: e.g., $t_v = t_q + \delta/2$ and $t'_q = t_v + \delta/2 = t_q + \delta$. Care must be taken to avoid numerical inaccuracy in case v_{x+1} becomes zero (in which case the update reduces to the normal leapfrog expression). Because the integration is exact, the results for the velocity Verlet and leapfrog algorithms are identical; velocity Verlet simply involves an intermediate update of one set of variables.

All of Jang and Voth’s algorithms can be derived as further approximations to this algorithm. Preliminary results suggest that Nosé–Hoover quasi-Hamiltonian conservation with this algorithm is similar to that with Jang and Voth’s algorithms.⁷²

There is a further intricacy in combining Nosé–Hoover dynamics (with any algorithm) with a multiple timestep algorithm such as RRESPA.³² Using RRESPA, the slow and fast forces are separated, and the slow forces are used to update the velocities only after several fast timesteps. In using RRESPA for Nosé–Hoover dynamics, the effects of Nosé–Hoover couplings on both slow and fast forces must be included without overcounting. We simply add the slow forces into one of the fast-force timesteps, multiplying the slow forces by the ratio of the slow and fast timesteps, and calculate the Nosé–Hoover dynamics for that short step using the combined forces.⁷³ This is not the only solution, but it does reduce to the appropriate limits in the absence of a Nosé–Hoover chain and if the same timestep is used for slow and fast forces, and it can be derived consistently using Trotter expansions.

Appendix B: Nonadiabatic Electron-Transfer Rate Constant with Coordinate-Dependent Electronic Coupling

If the electronic coupling V_{ij} is a known function of the system coordinates, but is still weak, the techniques described in section II A can be used to obtain a slightly more general expression for the electron-transfer rate constant. Starting from eq 2 one obtains

$$k_{\text{sp}} = \frac{1}{\hbar} \sqrt{\frac{2\pi\beta}{d^2 \ln A(\tau)/d\tau|_{\tau_{\text{ts}}}}} A(\tau_{\text{ts}}) \quad (\text{B1})$$

where

$$A(\tau) = \frac{1}{Z(0)} \text{Tr}[e^{-H_B\beta(1-\tau)} V_{ij} e^{-H_B\beta\tau} V_{ij}] \quad (\text{B2})$$

$Z(\tau)$ is defined in eq 6, and τ_{ts} is now defined by $dA(\tau)/d\tau|_{\tau_{\text{ts}}} = 0$.

$A(\tau)$ can be calculated using path integral molecular dynamics as the product of an average in the hybrid distribution with the exponential of the activation free energy

$$A(\tau) = \langle V_{ij}(\tau) V_{ij}(0) \rangle_\tau \exp[-\beta(F(\tau) - F(0))] \quad (\text{B3})$$

where $F(\tau)$ is defined in eq 6, and $\langle V_{ij}(\tau) V_{ij}(0) \rangle_\tau$ is defined in eq 9. The derivatives of $A(\tau)$ could be found numerically or could be directly calculated using the imaginary-time derivatives of the path integral representation of $A(\tau)$.

Appendix C: Nonadiabatic Electron-Transfer Rate Expressions for Harmonic Systems

The simply displaced harmonic or spin boson system consists of multidimensional harmonic potential energy surfaces in the two electronic states that are coupled and displaced but otherwise

identical, with no change in frequency or rotations: $V_i(\mathbf{x}) = \Sigma K_n x_n^2$, and $V_f(\mathbf{x}) = \Sigma K_n (x_n - \Delta_n)^2 + \epsilon$. As in Section IV C, K_n is the force constant and Δ_n is the displacement in mode x_n with frequency ω_n . For such a system in the Condon approximation, the integrand of eq 2 can be solved analytically:^{6,7} $k = V_{if}^2 \hbar^2 \int dt \exp[-\beta \Delta F(t)]$, where

$$\Delta F(t) = -\frac{1}{\beta} \ln \langle e^{iH_d t/\hbar} e^{-iH_f t/\hbar} \rangle_i = \frac{i\epsilon t}{\hbar\beta} + \sum_n \frac{K_n \Delta_n^2}{2\beta\hbar\omega_n} [\coth(\beta\hbar\omega_n/2)(1 - \cos(\omega_n t)) + i \sin(\omega_n t)] \quad (C1)$$

Here, $\Delta F(t)$ is the same as $\Delta F(\tau) = F(\tau) - F(0)$, where $F(\tau)$ is defined in eq 6, for $t = -i\hbar\beta\tau$. Thus one can immediately obtain $\Delta F(\tau)$ for the simply displaced harmonic system. After some trigonometric manipulation

$$\Delta F(\tau) = \epsilon\tau + \sum_n \frac{K_n \Delta_n^2}{2\beta\hbar\omega_n} \frac{\cosh(\beta\hbar\omega_n/2) - \cosh(\beta\hbar\omega_n(1/2 - \tau))}{\sinh(\beta\hbar\omega_n/2)} \quad (C2)$$

The derivatives with respect to τ can be readily derived. The classical limit equivalent to the classical simulations is not simply the limit of $Z(t)$ as $\beta\hbar\omega$ becomes small. That is a “dynamic” classical limit. The “static” classical expression is found by assuming that the exponents in the first expression for $\Delta F(t)$ in eq C1 commute and hence $\Delta F_{cl}(t) = -\ln\langle \exp(-i\Delta V t) \rangle/\beta$, or by taking the high-temperature limit of $F(\tau)$ in eq C2. Then $F(\tau)$ becomes a simple quadratic function

$$\Delta F_{cl}(\tau) = \epsilon\tau + \lambda(\tau - \tau^2) \quad (C3)$$

where $\lambda = \Sigma K_n \Delta_n^2/2$ is the reorganization free energy. In the classical limit both the real-time integral (eq 2) and the stationary phase approximation (eq 5) reduce to the Marcus expression (eq 3).

For a multidimensional harmonic system in which the frequencies are different and the minima displaced in the two electronic states, one can still obtain analytical expressions for $F(t)$ and $F(\tau)$, but the expressions become more complicated. The real-time expression is⁷⁴

$$\beta\Delta F(t) = \frac{i\epsilon t}{\hbar} - \sum_n \frac{im_n \Delta_n^2 \hbar}{\cot(\theta_{i,n})/\omega_{i,n} - \cot(\theta_{f,n}t/2)/\omega_{f,n}} + \frac{1}{2} \ln \left[\frac{4 \sinh^2(\beta\hbar\omega_{i,n}/2)\omega_{i,n}\omega_{f,n}}{(\omega_{i,n} - \omega_{f,n})^2 \sin^2(\theta_{i,n} + \theta_{f,n}) - (\omega_{i,n} + \omega_{f,n})^2 \sin^2(\theta_{i,n} - \theta_{f,n})} \right] \quad (C4)$$

where m_n is the mass of the mode ($m_n = 1$ if the coordinates are mass weighted), $\theta_{i,n} = \omega_{i,n}(t + i\hbar\beta)/2$, $\theta_{f,n} = \omega_{f,n}t/2$, and the mode frequencies refer to the initial or final electronic state. Again taking $t = -i\hbar\beta\tau$ yields⁷⁴

$$\Delta F(\tau) = \epsilon\tau + \sum_n \frac{m_n \Delta_n^2/(\hbar\beta)}{\coth(\theta'_{i,n})/\omega_{i,n} - \coth(\theta'_{f,n})/\omega_{f,n}} - \frac{1}{2\beta} \left[\frac{4 \sinh^2(\beta\hbar\omega_{i,n}/2)\omega_{i,n}\omega_{f,n}}{(\omega_{i,n} + \omega_{f,n})^2 \sinh^2(\theta'_{i,n} + \theta'_{f,n}) - (\omega_{i,n} - \omega_{f,n})^2 \sinh^2(\theta'_{i,n} - \theta'_{f,n})} \right] \quad (C5)$$

where $\theta'_{i,n} = \beta\hbar\omega_{i,n}(1 - \tau)/2$, and $\theta'_{f,n} = \beta\hbar\omega_{f,n}\tau/2$. Again one can take the static classical limit (here done differently than in ref 74)

$$\Delta F_{cl}(\tau) = \epsilon\tau + \lambda_f \tau - c_\tau \tau^2 - (1/\beta) \sum_n \ln(\omega_{i,n}/\omega_{\tau,n}) \quad (C6)$$

where $\lambda_f = \Sigma K_{f,n} \Delta_n^2/2$ (this is the reorganization energy, but not free energy, in the final state), $m_n \omega_{\tau,n}^2 = K_{\tau,n} = (1 - \tau)K_{i,n} + \tau K_{f,n}$, and $c_\tau = \Sigma K_{f,n}^2 \Delta_n^2/(2K_{\tau,n})$. $F_{cl}(\tau)$ is no longer a simple quadratic function of τ and hence does not simplify to the Marcus expression.

As discussed in section IV C, two spectral densities are needed to obtain parameters for a shifted frequency harmonic model, but there is no simple way to obtain the parameters from the spectral densities. We used the following procedure. On the basis of the similarity of the simulated spectral densities in the initial and final states (see Figure 4), we assumed that most modes do not shift frequencies. Only six modes representing the Co–ligand stretches and 15 modes representing the H–N–H bends were allowed frequency shifts. These modes were given frequencies spread evenly over their respective peaks, with a constant frequency shift for all of the modes in each peak based on the spectral shift. The coordinate displacement in each shifted frequency mode was the lesser of those derived from the two spectral densities; the spectral amplitudes at the mode frequencies were determined relative to the spectral baselines taken from the other spectrum. Displacements in the modes without frequency shifts were then determined from the spectral amplitude not accounted for by the shifted frequency modes (including the frequency-doubled components from the second term in eq 20), averaged over the two spectra.

References and Notes

- (1) Marcus, R. A.; Sutin, N. *Biochim. Biophys. Acta* **1985**, *811*, 265.
- (2) Marcus, R. A. *J. Chem. Phys.* **1956**, *24*, 966.
- (3) Valleau, J. P.; Torrie, G. M. In *Statistical Mechanics, Part A*; Berne, B. J., Ed.; Plenum Press: New York, 1977; pp 169–194.
- (4) Onuchic, J. N.; Beratan, D. N.; Hopfield, J. J. *J. Phys. Chem.* **1986**, *90*, 3707.
- (5) Jortner, J. *J. Chem. Phys.* **1976**, *64*, 4860.
- (6) Fischer, S. F. *J. Chem. Phys.* **1970**, *53*, 3195.
- (7) van Duyne, R. P.; Fischer, S. F. *J. Chem. Phys.* **1974**, *5*, 183.
- (8) Wolynes, P. G. *J. Chem. Phys.* **1987**, *87*, 6559.
- (9) Cao, J.; Voth, G. A. *J. Chem. Phys.* **1997**, *106*, 1769. Note that τ and ΔV are defined slightly differently here.
- (10) Bader, J. S.; Kuharski, R. A.; Chandler, D. *J. Chem. Phys.* **1990**, *93*, 230.
- (11) Zheng, C.; McCammon, J. A.; Wolynes, P. G. *Proc. Natl. Acad. Sci. U.S.A.* **1989**, *86*, 6441.
- (12) Zheng, C.; McCammon, J. A.; Wolynes, P. G. *J. Chem. Phys.* **1991**, *158*, 261.
- (13) Newton, M. D. *Chem. Rev.* **1991**, *91*, 767.
- (14) Cave, R. J.; Newton, M. D. *Chem. Phys. Lett.* **1996**, *249*, 15.
- (15) Yoshimura, A.; Nozaki, K.; Ikeda, N.; Ohno, T. *J. Phys. Chem.* **1996**, *100*, 1630. Yoshimura, A.; Nozaki, K.; Ohno, T. *Coord. Chem. Rev.* **1997**, *159*, 375.
- (16) Hupp, J. T.; Weaver, M. J. *Inorg. Chem.* **1984**, *23*, 256.
- (17) Matyushov, D. V. *J. Chem. Phys.* **1993**, *174*, 199.
- (18) Matyushov, D. V.; Schmid, R. *J. Phys. Chem.* **1994**, *98*, 5152. Matyushov, D. V.; Schmid, R. *Chem. Phys. Lett.* **1994**, *220*, 359.

- (19) Heitele, H.; Pöllinger, F.; Weeren, S.; Michel-Beyerle, M. E. *Chem. Phys. Lett.* **1990**, *168*, 598.
- (20) Isied, S. S.; Ogawa, M. Y.; Wishart, J. F. *Chem. Rev.* **1992**, *92*, 381.
- (21) Ogawa, M. Y.; Wishart, J. F.; Young, Z.; Miller, J. R.; Isied, S. S. *J. Phys. Chem.* **1993**, *97*, 11456.
- (22) Sneddon, S. F.; Brooks, C. L., III *J. Am. Chem. Soc.* **1992**, *114*, 8220.
- (23) Newton, M. D. *J. Phys. Chem.* **1991**, *95*, 30.
- (24) Brunschwig, B. S.; Creutz, C.; Macartney, D. H.; Sham, T.-K.; Sutin, N. *Faraday Discuss. Chem. Soc.* **1982**, *74*, 113.
- (25) Szalda, D. J.; Macartney, D. H.; Sutin, N. *Inorg. Chem.* **1984**, *23*, 3473.
- (26) Buhks, E.; Bixon, M.; Jortner, J.; Navon, G. *Inorg. Chem.* **1979**, *18*, 2014.
- (27) Kuharski, R. A.; Bader, J. S.; Chandler, D.; Sprik, M.; Klein, M. L.; Impey, R. W. *J. Chem. Phys.* **1988**, *89*, 3248.
- (28) Billing, R. *Coord. Chem. Rev.* **1997**, *159*, 257.
- (29) Billing, R., private communication.
- (30) Brunschwig, B. S.; Ehrenson, S.; Sutin, N. *J. Phys. Chem.* **1986**, *90*, 3657.
- (31) (a) Berne, B. J.; Thirumalai, D. *Ann. Rev. Phys. Chem.* **1986**, *37*, 401. (b) See also the related analysis of Zhou, H.-X.; Szabo, A. *J. Chem. Phys.* **1995**, *103*, 3481.
- (32) Tuckerman, M.; Berne, B. J.; Martyna, G. J. *J. Chem. Phys.* **1990**, *97*, 1990.
- (33) Anderson, H. C. *J. Chem. Phys.* **1980**, *72*, 2384.
- (34) Brooks, B. R.; Bruccoleri, R. E.; Olafson, B. D.; States, D. J.; Swaminathan, S.; Karplus, M. *J. Comput. Chem.* **1983**, *4*, 187.
- (35) Zerner, M. C.; Loew, G. H.; Kirchner, R. F.; Mueller-Westerhoff, U. T. *J. Am. Chem. Soc.* **1980**, *102*, 589.
- (36) A comprehensive semiempirical SCF/CI package written by M. C. Zerner and co-workers, University of Florida, Gainesville, FL.
- (37) Newton, M. D.; Ohta, K.; Zhong, E. *J. Phys. Chem.* **1991**, *95*, 2317.
- (38) Cave, R. J.; Newton, M. D.; Kumer, K.; Zimmt, M. B. *J. Phys. Chem.* **1995**, *99*, 17501.
- (39) Sachs, S. B.; Dudek, S. P.; Hsung, R. P.; Sita, L. R.; Smalley, J. F.; Newton, M. D.; Feldberg, S. W.; Chidsey, C. E. D. *J. Am. Chem. Soc.* **1997**, *119*, 10563.
- (40) Song, X.; Lei, Y.; Van Wallendael, S.; Perkovic, M. W.; Jackman, D. C.; Endicott, J. F.; Rillema, D. P. *J. Phys. Chem.* **1993**, *97*, 3225.
- (41) The Mulliken charges refer to a nonorthogonal basis of Slater-type orbitals and are considered to be physically more appropriate than the analogous charges on the basis of the implicit orthonormal atomic orbitals of the INDO/s model. See, e.g., ref 75.
- (42) Zeng, J.; Hush, N. S.; Reimers, J. R. *J. Phys. Chem.* **1995**, *99*, 10459. Contains a recent example of the use of INDO/s atomic charges in modeling electron transfer involving transition metal complexes.
- (43) Biner, M.; Bürgi, H.-B.; Ludi, A.; Röhr, C. *J. Am. Chem. Soc.* **1992**, *114*, 5197.
- (44) Bagger, S.; Kristjansson, I.; Sotøfte, I.; Thorlacius, A. *Acta. Chem. Scand. A* **1985**, *39*, 125.
- (45) Schmidt, K. H.; Müller, A. *Inorg. Chem.* **1975**, *14*, 2183.
- (46) Kumar, S.; Bouzida, D.; Swendsen, R. H.; Kollman, P. A.; Rosenberg, J. M. *J. Comput. Chem.* **1992**, *13*, 1011.
- (47) Lynden-Bell, R. M.; Rasaiah, J. C. *J. Chem. Phys.* **1997**, *107*, 1981.
- (48) Levy, R. M.; Gallicchio, E. *Ann. Rev. Phys. Chem.* **1998**, *49*, 531.
- (49) The entropy also could be calculated directly from simulations using
- $$\frac{dS}{d\tau} = \frac{1}{T} \left(\frac{dE}{d\tau} - \frac{dF}{d\tau} \right) = \frac{\beta}{T} (\langle \Delta V(\tau) H_{\tau}(0) \rangle_{\tau} - \langle \Delta V \rangle_{\tau} \langle H_{\tau} \rangle_{\tau})$$
- (50) Marcus, R. A.; Sutin, N. *Comments Inorg. Chem.* **1986**, *5*, 119.
- (51) Harris, F. J. *Proc. IEEE* **1978**, *66*, 51.
- (52) Kneifel, C. L.; Newton, M. D.; Friedman, H. L. *J. Mol. Liq.* **1994**, *60*, 107.
- (53) Leggett, A. J.; Chakravarty, S.; Dorsey, A. T.; Fisher, M. P. A.; Garg, A.; Zwerger, W. *Rev. Mod. Phys.* **1987**, *59*, 1.
- (54) Because the terms are sometimes used differently, it may be useful to clarify our usage here. "Harmonic" refers to the potential energy surfaces in a given electronic state. The "simply displaced harmonic" model has parabolic free energy curves ($F(\tau)$ and $F(x)$) as well as parabolic potentials. The "shifted frequency harmonic" model is nonlinear and thus does not in general have parabolic free energy curves.
- (55) Richardson, D. E.; Sharpe, P. *Inorg. Chem.* **1991**, *30*, 1412.
- (56) Song, X.; Marcus, R. A. *J. Chem. Phys.* **1993**, *99*, 7768.
- (57) Isied, S. S.; Vassilian, A.; Wishart, J. F.; Creutz, C.; Schwarz, H. A.; Sutin, N. *J. Am. Chem. Soc.* **1988**, *110*, 635.
- (58) Pekar, S. *Investigations of the Electric Theory of Crystals*, 1951, US AEC document AEC-tr-5575.
- (59) *Handbook of Chemistry*, 10th ed.; Lange, N. A., Ed.; McGraw-Hill: New York, 1967.
- (60) Liu, Y. P.; Newton, M. D. *J. Phys. Chem.* **1995**, *99*, 12382.
- (61) Bader, J. S.; Berne, B. J. *J. Chem. Phys.* **1996**, *104*, 1293.
- (62) This continuum result was obtained as the difference of two calculations carried out with the DelPhi code:⁷⁶ (1) The total λ_s , based on full solvation beyond the system cavity; and (2) the contribution to λ_s from solvation beyond the 10.1 Å shell surrounding the system cavity.
- (63) Warshel, A.; Hwang, J.-K. *J. Chem. Phys.* **1986**, *84*, 4936.
- (64) We note that the quantum suppression is of the activation free energy and thus includes any entropic contribution to nuclear tunneling, and that it is not corrected for limitations of the solvent model.
- (65) An additional source of uncertainty in the calculated results is the value adopted for ΔF° , taken here as -13.8 kcal/mol and estimated as -15.4 kcal/mol using the data of refs 21 and 29. Assuming an uncertainty of ± 2 kcal/mol would lead to an uncertainty of ~ 1 kcal/mol in ΔF^\ddagger and a similar uncertainty in ΔE^\ddagger .
- (66) Richardson, D. E.; Sharpe, P. *Inorg. Chem.* **1993**, *32*, 1809.
- (67) Hummer, G.; Pratt, L. R.; Garcia, E. *J. Phys. Chem. A* **1998**, *102*, 7885.
- (68) Nosé, S. *Mol. Phys.* **1984**, *52*, 255.
- (69) Hoover, W. G. *Phys. Rev. A* **1985**, *31*, 1695.
- (70) Martyna, G. J.; Klein, M. L.; Tuckerman, M. *J. Chem. Phys.* **1992**, *97*, 2635.
- (71) Jang, S.; Voth, G. A. *J. Chem. Phys.* **1997**, *107*, 9514.
- (72) Jang, S., unpublished results.
- (73) Tuckerman, M.; Berne, B. J.; Martyna, G. J.; Klein, M. L. *J. Chem. Phys.* **1993**, *99*, 2796.
- (74) Tang, J. *Chem. Phys.* **1994**, *188*, 143.
- (75) Pearl, G. M.; Zerner, M. C. *J. Am. Chem. Soc.* **1999**, *121*, 399.
- (76) Sharp, K. A.; Nicholls, A., *DelPhi*, v3.0, 1989. Sharp, K.; Honig, B. *Annu. Rev. Biophys. Biophys. Chem.* **1990**, *19*, 301.
- (77) Kraulis, P. J. *J. Appl. Crystallogr.* **1991**, *24*, 946.
- (78) Merritt, E. A.; Bacon, D. J. *Methods Enzymol.* **1997**, *277*, 505.